JOURNAL OF GEOPHYSICAL RESEARCH, VOL. 97, NO. C12, PAGES 20,201–20,226, DECEMBER 15, 1992

Three-Dimensional Analytical Model for the Mixed Layer Depth

XIAO-HAI YAN

Center for Remote Sensing, Graduate College of Marine Studies, University of Delaware, Newark

AKIRA OKUBO

Marine Sciences Research Center, State University of New York, Stony Brook

We have recently developed a three-dimensional semi-analytical mixed layer remote sensing model which includes the horizontal advection and diffusion processes in our previous one dimensional model (*Yan et al.*, 1991a). The three-dimensional (3-D) model can be used as a supplement to the one-dimensional (1-D) model in the area where advection is important and for a finer resolution grid prediction. The 3-D thermal inertia model is based on the 3-D thermal energy conservation equation. Using sine transformation and inverse sine transformation methods, we obtained the solution for mixed layer thermal inertia which, in turn, can be used to calculate mixed layer depth using a similar method to that of Yan et al. (1991a). In the solution, the thermal inertia (which is proportional to the mixed layer depth) is expressed as functions of sea surface temperature changes (δSST), heat flux (Q) and surface layer velocity (u, v, and w). The vertical entrainment and wind effects are accounted for in the model by eddy diffusivity while changes of δSST result from entrainment, e.g., if vertical entrainment is larger, δSST will be smaller and vice versa. The advantages of this model are that it can be easily forced by remotely sensed data and that it is much simpler to compute than numerical 3-D mixed layer turbulence closure models. The model was tested using the data from the advanced very high resolution radiometer/multichannel sea surface temperature data set and the Cooperative Ocean Atmosphere Data Set for the North Pacific Ocean. The model-predicted mixed layer depths compared favorably with the mixed layer depths calculated from 14 years of Volunteer Observing Ship/expendable bathythermograph observation data. The model/data comparison also exhibited a number of mesoscale features of seasonal changes and anomalies of the mixed layer depth.

INTRODUCTION

The mixed layer depth determines both the thermal and the mechanical inertia of the layer in direct contact with the atmosphere [*Yan et al.*, 1989, 1990*a*]; hence it affects the oceanic response to the prescribed surface forcing and the evolution of the coupled ocean-atmosphere system. Thus the study of mixed layer depth and its variability is of great importance for the understanding and interpretation of thermal and velocity fields of the upper ocean, for parameterizing mixed layer processes, and for air-sea interaction.

Since 1979, remotely sensed data (e.g., advanced very high resolution radiometer (AVHRR)) have been used to identify ocean phenomena which produce a near-surface signature detectable from space. Often, such data are combined with shipboard observations to study the structure and dynamics of the upper ocean. For example, coastal streamers [e.g., *Flament et al.*, 1985] and mesoscale eddies in the California current system [e.g., *Simpson and Lynn*, 1990] have been studied with such combinations of data. These combined data sets utilize the large-scale, synoptic nature of remotely sensed observations to their advantage while simultaneously overcoming the principal limitation of remotely sensed data, namely, that sensed observations (e.g., AVHRR) typically provide little direct information on the interior ocean.

Generally, models of the upper ocean response to wind forcing and heat flux have relied more on in situ data than on remotely sensed data [e.g., *Mellor and Yamada*, 1974; *Price et al.*, 1986]. More recently, however, combinations of remotely sensed and in situ data also have been used to initialize, force, and validate numerical models and analytical models of mixed layer processes. For example, AVHRR and Scanning Multichannel Microwave Radiometer (SMMR) data have been used with both turbulence closure [*Yan et al.*, 1990*a,b*] and thermal inertia [*Yan et al.* 1991*a,b*] models to predict mixed layer depth in the northwest Sargasso Sea.

All the model studies cited above have assumed that vertical mixing is the dominant mixing process in the upper ocean and that horizontal advection is negligible. These assumptions may be true, at least in the mid-ocean away from frontal zones. In major current systems (e.g., California current system) and in the regions of ocean where variations in the thermal structure of the upper layer due to horizontal advection are large, the simulation of the mixed layer depth is much more complicated. *Blumberg and Mellor* [1987] developed a three-dimensional, primitive equations, time-dependent, coastal circulation model with a sophisticated turbulence closure scheme. Because the turbulence submodel is also three-dimensional and the mean fields are computed with the same resolution as for turbulent quantities, the computational time for the model could be exorbitant for long-term integration. Since advective processes do not need a vertical resolution as high as that needed for boundary mixing processes, computational efficiency could be obtained if these two processes were computed separately or if an analytical scheme could be obtained. The major limitation of observational studies (i.e., mesoscale and small-scale process-oriented experiments) which have combined in

Paper number 92JC01833.
0148-0227/92/92JC-01833$05.00

situ data with remotely sensed data generally has been that only isolated realizations of more general ocean processes have been examined in detail. Placing such studies within the context of large-scale circulation can, on occasion, be difficult because large-scale, synoptic observations often are not available.

Yan et al. [1990*a*, 1991*a*] described a one-dimensional mixed layer thermal inertia (MLTI) model to estimate the thermal inertia of the mixed layer and daily mean mixed layer depth using satellite data. The basis of the MLTI model is that the daily (or monthly) sea surface temperature change (δSST) is primarily a function of the net heat flux at the sea surface and the thermal inertia, and that the daily mean (or monthly mean) mixed layer depth can be determined from the thermal inertia.

In this paper, we propose a three-dimensional semi-analytical MLTI model which includes the horizontal advection and diffusion terms in our previous one-dimensional model. The three-dimensional thermal inertia model is based on the three-dimensional thermal energy conservation equation. Using sine transformation and inverse sine transformation methods, we obtain the solution for MLTI which can be used to calculate mixed layer depth using a similar method to that of *Yan et al.* [1991*a*]. In the solution, the thermal inertia, which is proportional to the mixed layer depth, is expressed as a function of δSST, net heat flux (Q), and a dimensionless number X (dependent on dimensionless variables relating to horizontal coordinates and times of maximum and minimum sea surface temperature). The vertical entrainment effects will be accounted for in the model by eddy diffusivity, while changes of δSST result from entrainment. For example, if vertical entrainment is larger, δSST will be smaller, and vice versa.

This three-dimensional thermal inertia model can also be easily forced by satellite data and is much simpler to compute than the numerical three-dimensional primitive equation-turbulence closure model. The model was tested using the data from the AVHRR-multichannel sea surface temperature (MCSST) data set, Geosat altimeter data set, and the Cooperative Ocean-Atmosphere Data Set (COADS) for the North Pacific Ocean. The model predicted mixed layer depths compared favorably with the mixed layer depths calculated from 14 years of Volunteer Observing Ship/expendable bathythermograph (VOS-XBT) observation data. The model/data comparisons also exhibited a number of meso-scale features of seasonal changes and anomalies of the mixed layer depth in the North Pacific Ocean. In the next sections, we will discuss the model and the results of the model test.

THREE DIMENSIONAL ANALYTICAL MODEL FOR MIXED LAYER DEPTH

Our model is based on the three-dimensional thermal energy conservation equation (6) of *Yan et al.* [1990a]:

$$\frac{\partial T}{\partial t} = -u\frac{\partial T}{\partial x} - v\frac{\partial T}{\partial y} - w\frac{\partial T}{\partial z} + K_m\frac{\partial^2 T}{\partial z^2} + \frac{\partial}{\partial x}\left(K_x\frac{\partial T}{\partial x}\right)$$

$$+ \frac{\partial}{\partial y}\left(K_y\frac{\partial T}{\partial y}\right) + \frac{\partial}{\partial z}\left(K_z\frac{\partial T}{\partial z}\right) - \frac{1}{C_P\rho}\frac{\partial I}{\partial z} \qquad (1)$$

where T is the seawater temperature, t is time, u, v, and w are the x, y, z components of an advection current, K_m is the molecular diffusivity, K_x, K_y are horizontal turbulent diffusivities for T, K_z is vertical turbulent diffusivity, ρ is the density of seawater, C_P is the heat capacity of sea water, and I is the downward flux of solar radiation.

For simplicity, we assume the following.

1. The advection current is uniform in a spatial domain of model grid and steady for the time interval of integration. In fact, the calculated current field is depth-dependent, but we take depth-averaged values for u and v.

2. The turbulent diffusivities are depth-averaged and treated as a constant for a short time period [*Yan et al.*, 1990*a*, 1991*a*].

3. The downward flux of solar radiation in the water column and molecular thermal conduction are ignored; *Yan et al.* [1990*a*] already demonstrated in the 1-D model that the effect of downward flux is negligibly small on the estimation of mixed layer depth.

Under these assumptions, (1) is reduced to

$$\frac{\partial T}{\partial t} = -u\frac{\partial T}{\partial x} - v\frac{\partial T}{\partial y} - w\frac{\partial T}{\partial z}$$

$$+ K_x\frac{\partial^2 T}{\partial x^2} + K_y\frac{\partial^2 T}{\partial y^2} + K_z\frac{\partial^2 T}{\partial z^2} \qquad (1')$$

Eq. (1′) is subject to the initial and boundary conditions:
At $t = 0$

$$T = T_0(x, y, z) \qquad (2)$$

(specified in the problem).
At $x = 0$

$$T = T_{11}(y, z, t) \qquad (3)$$

(specified in the problem).
At $x = L_x$

$$T = T_{12}(y, z, t) \qquad (4)$$

(specified in the problem).
At $y = 0$

$$T = T_{21}(x, z, t) \qquad (5)$$

(specified in the problem).
At $y = L_y$

$$T = T_{22}(x, z, t) \qquad (6)$$

(specified in the problem).
At $z = 0$ (sea surface)

$$(wT)_{z=0} + (-K_z\frac{\partial T}{\partial z})_0 = a(t) - (M + N^*T)_{z=0} \qquad (7)$$

At z = D (certain deep depth)

$$T = T_D \text{ (const)}. \qquad (8)$$

An analytical solution of (1′) subject to (2)–(8) is obtained by (see appendix for details)

$$T(x,y,z,t) = \exp\left[\left(\frac{u}{2K_x}x - \frac{u^2}{4K_x}t\right)\right.$$

$$\left. + \left(\frac{v}{2K_y}y - \frac{v^2}{4K_y}t\right) + \left(\frac{w}{2K_z}z - \frac{w^2}{4K_z}t\right)\right] \cdot$$

$$\frac{4}{L_x L_y}\sum_{k=1}^{\infty}\sum_{m=1}^{\infty} \sin\left(\frac{k\pi}{L_x}x\right)$$

$$\sin\left(\frac{m\pi}{L_y}y\right) e^{\left(\frac{k^2\pi^2}{L_x^2}K_x + \frac{m^2\pi^2}{L_y^2}K_y\right)t}$$

$$\left\{\tilde{A}(t)e^{\frac{N}{K_z}z} + e^{\frac{N}{K_z}z}\right.\cdot$$

$$\left.\int_o^z \left(-\frac{N}{K_z}\right)\phi(z',t)e^{-\frac{N}{K_z}z'}dz'\right\} \tag{9}$$

where

$$N = N^* + \frac{\dot{w}}{2} \tag{10}$$

$$\tilde{A}(t) = \tilde{C}_D e^{-\frac{N}{K_z}D} e^{\left(\frac{k^2\pi^2}{L_x^2}K_x + \frac{m^2\pi^2}{L_y^2}K_y\right)t}$$

$$+ \frac{N}{K_z}\int_o^D \phi(z',t)e^{-\frac{N}{K_z}z'}dz' \tag{10'}$$

and

$$\tilde{C}_D = T_D e^{\left(\frac{u^2}{4K_x} + \frac{v^2}{4K_y} + \frac{w^2}{4K_z}\right)t} e^{-\frac{w}{2K_z}D}$$

$$\int_o^{L_x}\int_o^{L_y} e^{-\frac{u}{2K_x}x - \frac{v}{2K_y}y} \sin\left(\frac{k\pi}{L_x}x\right) \sin\left(\frac{m\pi}{L_y}y\right) dxdy \tag{11}$$

with

$$\phi(z,t) = \frac{2}{D}\sum_{n=1}^{\infty} e^{-\frac{n^2\pi^2}{D^2}K_z t} \sin\frac{n\pi}{D}z \int_o^D \phi_o(z')\cdot$$

$$\sin\frac{n\pi}{D}z'dz' + \frac{2\pi}{D^2}K_z\sum_{n=1}^{\infty} n e^{-\frac{n^2\pi^2}{D^2}K_z t}\sin\frac{n\pi}{D}z$$

$$\int_o^t e^{\frac{n^2\pi^2}{D^2}K_z t'}\left(B_o(t') - (-1)^n B_D(t')\right)dt'$$

$$+\frac{2}{D}\sum_{n=1}^{\infty} e^{-\frac{n^2\pi^2}{D^2}K_z t}\sin\frac{n\pi}{D}z$$

$$\int_o^t e^{\frac{n^2\pi^2}{D^2}K_z t'}dt'\int_o^D R(z',t')\sin\frac{n\pi}{D}z'dz'$$

$$-\frac{2\pi}{D^2 N}K_z\sum_{n=1}^{\infty} e^{-\frac{n^2\pi^2}{D^2}K_z t}\sin\frac{n\pi}{D}z$$

$$\int_o^t e^{\frac{n^2\pi^2}{D^2}K_z t'}dt'\int_o^D R(z',t')\cos\frac{n\pi}{D}z'dz' \tag{11'}$$

$$\phi_o(z) = \tilde{C}_o(z;k,m) - \frac{K_z}{N}\frac{\partial}{\partial z}\left(\tilde{C}_o(z;k,m)\right) \tag{12}$$

$$\tilde{C}_o = \int_o^{L_x}\int_o^{L_y} T_o(x,y,z)e^{-\frac{u}{2K_x}x - \frac{v}{2K_y}y - \frac{w}{2K_z}z}$$

$$\sin\left(\frac{k\pi}{L_x}x\right)\sin\left(\frac{m\pi}{L_y}y\right)dxdy \tag{13}$$

$$B_o(t) = \frac{\alpha(t)}{N}e^{\left(\frac{k^2\pi^2}{L_x^2}K_x + \frac{m^2\pi^2}{L_y^2}K_y\right)t} \tag{14}$$

$$\frac{\alpha(t)}{N} = \frac{(a(t) - M)}{N}e^{\left(\frac{u^2}{4K_x} + \frac{v^2}{4K_y} + \frac{w^2}{4K_z}\right)t}$$

$$\int_o^{L_x}\int_o^{L_y} e^{-\frac{u}{2K_x}x - \frac{v}{2K_y}y}\sin\left(\frac{k\pi}{L_x}x\right)\sin\left(\frac{m\pi}{L_y}y\right)dxdy \tag{15}$$

$$B_D(t) = \tilde{C}_D e^{\left(\frac{k^2\pi^2}{L_x^2}K_x + \frac{m^2\pi^2}{L_y^2}K_y\right)t} \tag{16}$$

$\tilde{C}_D$ is given by (11)

$$R(z,t) = \left[\frac{k\pi}{L_x}K_x\left((-1)^k C_{12}^* - C_{11}^*\right)\right.$$

$$\left. + \frac{m\pi}{L_Y}K_y\left((-1)^m C_{22}^{**} - C_{21}^{**}\right)\right] e^{\left(\frac{k^2\pi^2}{L_x^2}K_x + \frac{m^2\pi^2}{L_y^2}K_y\right)t} \tag{17}$$

$$C_{12}^* = \int_o^{L_y} T_{12}(y,z,t)e^{-\frac{v}{2K_y}y - \frac{w}{2K_z}z}\cdot$$

$$e^{-\frac{u}{2K_x}L_x}e^{\left(\frac{u^2}{4K_x} + \frac{v^2}{4K_y} + \frac{w^2}{4K_z}\right)t}\sin\left(\frac{m\pi}{L_y}y\right)dy \tag{18}$$

$$C_{11}^* = \int_o^{L_y} T_{11}(y,z,t)e^{-\frac{v}{2K_y}y - \frac{w}{2K_z}z}\cdot$$

$$e^{\left(\frac{u^2}{4K_x} + \frac{v^2}{4K_y} + \frac{w^2}{4K_z}\right)t}\sin\left(\frac{m\pi}{L_y}y\right)dy \tag{19}$$

$$C_{22}^* = \int_o^{L_x} T_{22}(x,z,t)e^{-\frac{u}{2K_x}x - \frac{w}{2K_z}z - \frac{v}{2k_y}L_y}\cdot$$

$$e^{\left(\frac{u^2}{4K_x} + \frac{v^2}{4K_y} + \frac{w^2}{4K_z}\right)t}\sin\left(\frac{k\pi}{L_x}x\right)dx \tag{20}$$

$$C_{21}^* = \int_o^{L_x} T_{21}(x,z,t)e^{-\frac{u}{2K_x}x - \frac{w}{2K_z}z}\cdot$$

$$e^{\left(\frac{u^2}{4K_x} + \frac{v^2}{4K_y} + \frac{w^2}{4K_z}\right)t}\sin\left(\frac{k\pi}{L_x}x\right)dx \tag{21}$$

The final expression of $T(x,y,z,t)$ is obtained from (9) by substituting (10)–(21). For simplicity, the turbulent diffusivities are depth-averaged and treated as a constant for a short time period in the model; the temperature distribution obtained from (9) does not have a vertical profile that looks like a mixed layer. However, the mixed layer depth can be obtained through the linear regression, since it is proportional to the thermal inertia [*Yan et al.*, 1991*a*].

By setting $z = 0$, (9) reads

$$T(x,y,o,t) \equiv SST(x,y,t) =$$

$$\exp\left[\left(\frac{u}{2K_x}x - \frac{u^2}{4K_x}t\right) + \left(\frac{v}{2K_y}y - \frac{v^2}{4K_y}t\right) + \left(-\frac{w^2}{4K_z}t\right)\right]\cdot$$

$$\frac{4}{L_xL_y}\sum_{k=1}^{\infty}\sum_{m=1}^{\infty} \sin\left(\frac{k\pi}{L_x}x\right) \sin\left(\frac{m\pi}{L_y}y\right)$$

$$\cdot\, e^{-\left(\frac{k^2\pi^2}{L_x^2}K_x + \frac{m^2\pi^2}{L_y^2}K_y\right)t}\left[\tilde{A}(t)\right] \tag{22}$$

Let us examine $\tilde{A}(t)$ more precisely. Taking (10), substituting (11) and (A34), using (A26) and (A27), and breaking α (in (A18)) into a part containing $a(t)$ and the rest, we obtain

$$\tilde{A}(t) = T_D O_{km}\exp$$

$$\left[\left(\frac{u^2}{4K_x} + \frac{v^2}{4K_y} + \frac{w^2}{4K_z} + \frac{k^2\pi^2}{L_x^2}K_x + \frac{m^2\pi^2}{L_y^2}K_y\right)t\right.$$

$$\left.-\frac{w}{2K_z}D - \frac{N}{K_z}D\right] + \frac{N}{K_z}\int_0^D dz' e^{-\frac{N}{K_z}z'}$$

$$\left[\frac{2}{D}\sum_{m=1}^{\infty} e^{-\frac{n^2\pi^2}{D^2}K_z t} \sin\left(\frac{n\pi}{D}z'\right)\right.$$

$$\left\{\int_0^D \phi_0(z'') \sin \frac{n\pi}{D}z'' dz''\right.$$

$$\left. + \int_0^t e^{\frac{n^2\pi^2}{D^2}K_z t'}dt' \int_0^D R(z'',t'') \sin \frac{n\pi}{D}z'' dz''\right\}$$

$$-\frac{2\pi}{D^2}K_z\sum_{n=1}^{\infty} ne^{\frac{-n^2\pi^2}{D^2}K_z t} \sin\left(\frac{n\pi}{D}z'\right)\cdot$$

$$\int_0^t e^{\frac{n^2\pi^2}{D^2}K_z t'}dt'\left\{(-1)^n B_D(t') + \frac{1}{nN}\int_0^D R(z'',t)\right.$$

$$\cos\left(\frac{n\pi}{D}z''\right)dz'' + \frac{M}{N}O_{km}\exp$$

$$\left.\left.\left(\left(\frac{u^2}{4K_z} + \frac{v^2}{4K_y} + \frac{w^2}{4K_z} + \frac{k^2\pi^2}{L_x^2}K_x + \frac{m^2\pi^2}{L_y^2}K_y\right)t'\right)\right\}\right]$$

$$+O_{km}\frac{2\pi N}{D^2}\int_0^D dz' e^{-\frac{N}{K_z}z'}\sum_{n=1}^{\infty} ne^{\frac{-n^2\pi^2}{D^2}K_z t}$$

$$\sin\left(\frac{n\pi}{D}z'\right)\int_0^t e^{\left(\frac{n^2\pi^2}{D^2}K_z + \frac{k^2\pi^2}{L_x^2}K_x + \frac{M^2\pi^2}{L_y^2}K_y\right)t'}$$

$$\frac{\alpha(t')}{N}e^{\left(\frac{u^2}{4K_z} + \frac{v^2}{4K_y}24 + \frac{w^2}{4K_z}\right)t'}dt' \tag{23}$$

In (23) we define

$$O_{km} \equiv \int_o^{L_x}\int_o^{L_y} e^{-\frac{u}{2K_x}x - \frac{v}{2K_y}y}$$

$$\sin\left(\frac{k\pi}{L_x}x\right) \sin\left(\frac{m\pi}{L_x}y\right) dxdy \tag{24}$$

Note that if $u = v = w = 0, L_x \to \infty, L_y \to \infty$, or $K_x = K_y = 0$, and SST is reduced to the same formula as given in *Yan et al.* [1991*a*].

When we substitute (23) into (22), we obtain the expression of SST, which consists of two parts: one part independent of $a(t) \equiv Q(t)/C_p\rho$, and the other part dependent on $a(t) = Q(t)/C_p\rho$. In other words, we can express

$$SST(x,y,t) = (SST)^*(x,y,t) + SST(t,Q(t);x,y) \tag{25}$$

where $(SST)^*$ represents the sea surface temperature contributed by the horizontal processes and vertical mixing without the heat source effect and where $SST(t,Q(t);x,y)$ represents the sea surface temperature contributed by the horizontal processes and vertical mixing with the surface heating effect.

Note that at any given location $(x,y), SST^*$ and $SST(t,Q(t);x,y)$ depend only on time.

The sea surface temperature range δSST can be obtained using:

$$\delta SST = SST(x,y,t_2) - SST(x,y,t_1) \tag{26}$$

In particular the part of δSST due to surface heating and cooling is given by

$$(\delta SST)_Q = SST(t_2,Q(t);x,y) - SST(t_1,Q(t);x,y) \tag{27}$$

Scaling Q, N, D, Z and t by $\hat{Q}, (K_z w)^{1/2}, (K_z/w)^{1/2}$, and w^{-1} respectively, where $\hat{Q}$ is the mean heat flux and ω is the frequency of heat flux variation, we can express (27) as

$$(\delta SST)_Q = \frac{\hat{Q}}{(\omega K_z)^{1/2}C_p\rho}\chi = \frac{\hat{Q}}{\omega^{1/2}[TI]}\chi \tag{28}$$

where $[TI] \equiv K_z^{1/2}C_p\rho$ (thermal inertia) and χ is a dimensionless number (dependent on dimensionless variables relating to horizontal coordinates and times of maximum and minimum sea surface temperature). Specifically,

$$\chi = 8\pi e^{u_1(\zeta - u_1\lambda\tau_M) + v_1(\xi - v_1\mu\tau_M) + w_1(-w_1\nu\tau_M)}$$

$$\sum_{k=1}^{\infty}\sum_{m=1}^{\infty} \sin(k\pi\xi) \sin(m\pi\xi) e^{-(k^2\pi^2\lambda + m^2\pi^2\mu)\tau_M}$$

$$\int_0^{'}\int_0^{'} e^{-u_1\zeta' - v_1\xi'} \sin(k\pi\xi) \sin(m\pi\xi')d\zeta' d\xi'\cdot$$

$$\int_0^{'} d\eta e^{-N'\eta}\sum_{n=1}^{\infty} ne^{-n^2\pi^2\tau_M} \sin(n\pi\eta)$$

$$\int_0^{\tau_M} e^{(n^2\pi^2 + k^2\pi^2\lambda + m^2\pi^2\mu + u_1^2\lambda + v_1^2\mu + w_1^2\nu)\tau'}Q'(\tau')d\tau'$$

$$-8\pi e^{u_1(\zeta - u_1\lambda\tau_m) + v_1(\xi - v_1\mu\tau_M) + w_1(-w_1\nu\tau_M)}$$

$$\sum_{k=1}^{\infty}\sum_{m=1}^{\infty} \sin(k\pi\zeta)\sin(m\pi\xi)e^{-(k^2\pi^2\lambda+m^2\pi^2\mu)\tau_m}$$

$$\int_0^1\int_0^1 e^{-u_1'\zeta'-v_1\xi'}\sin(k\pi\zeta')\sin(m\pi\xi')d\zeta'd\xi'\cdot$$

$$\int_0^1 d\eta e^{-N'\eta}\sum_{n=1}^{\infty} ne^{-n^2\pi^2\tau_m}\sin(n\pi\eta)$$

$$\int_0^{\tau_m} e^{(n^2\pi^2+k^2\pi^2\lambda+m^2\pi^2\mu+u_1^2\lambda+v_1^2\mu+w_1^2\nu)\tau'}Q'(\tau')d\tau' \quad (29)$$

where $Q' \equiv Q(t)/\hat{Q}$, $N' \equiv N/(K_z\omega)^{1/2}$, $u_1 \equiv uL_x/2K_x, v_1 \equiv vL_y/2K_y, w_1 \equiv w_D/2K_z$, $\lambda \equiv K_x/L_x^2\omega, \mu \equiv K_y/L_y^2\omega$, $\nu \equiv K_z/D^2\omega$, $\zeta \equiv x/L_x$, $\xi \equiv y/L_y$, $\eta \equiv Z/D$, $\tau \equiv \omega t$ and τ_M and τ_m denote the dimensionless times at which the sea surface temperature exhibits its maximum and minimum, respectively. Again, if $u = v = w = 0$, $L_x \to \infty$, $L_y \to \infty$ or $K_x = K_y = 0$, χ is reduced to the same formula as given by *Yan et al.* [1991*a*].

DATA SET AND ANALYSIS METHODOLOGY

Observation (Sea Truth) Data and Processing Method

The sea truth data used to verify the model results in this study were collected for 14 years (1976-1989) by volunteer ships in the North Pacific Ocean using XBT's along their routes. The data consist of 245,000 XBT observations in the form of monthly data files. The data consist essentially of temperature values at arbitrary depths at a number of points in the area 20°N to 55°N; 100°E to 120°W. The temperature

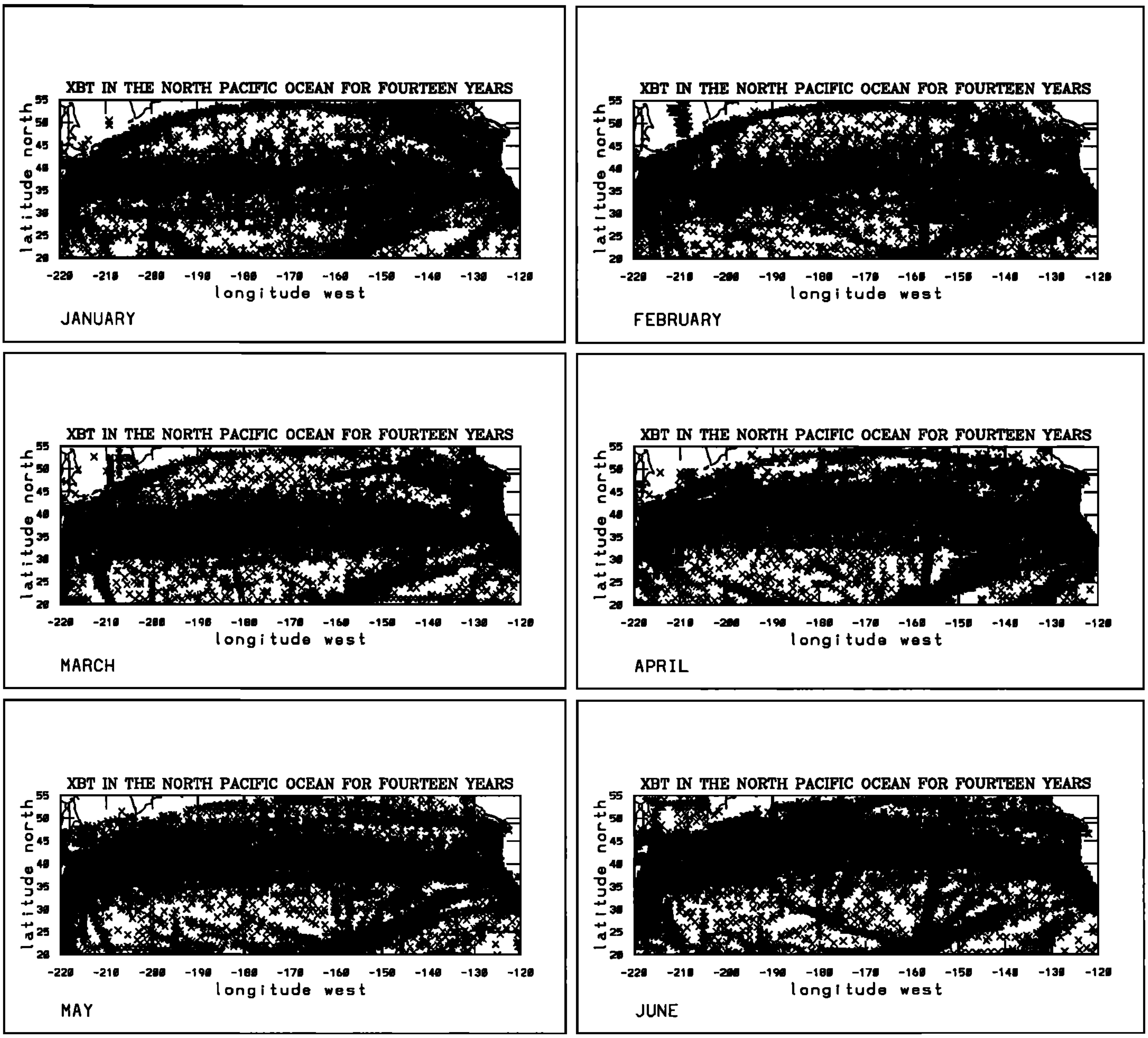

Fig. 1. VOS-XBT data points in the North Pacific Ocean.

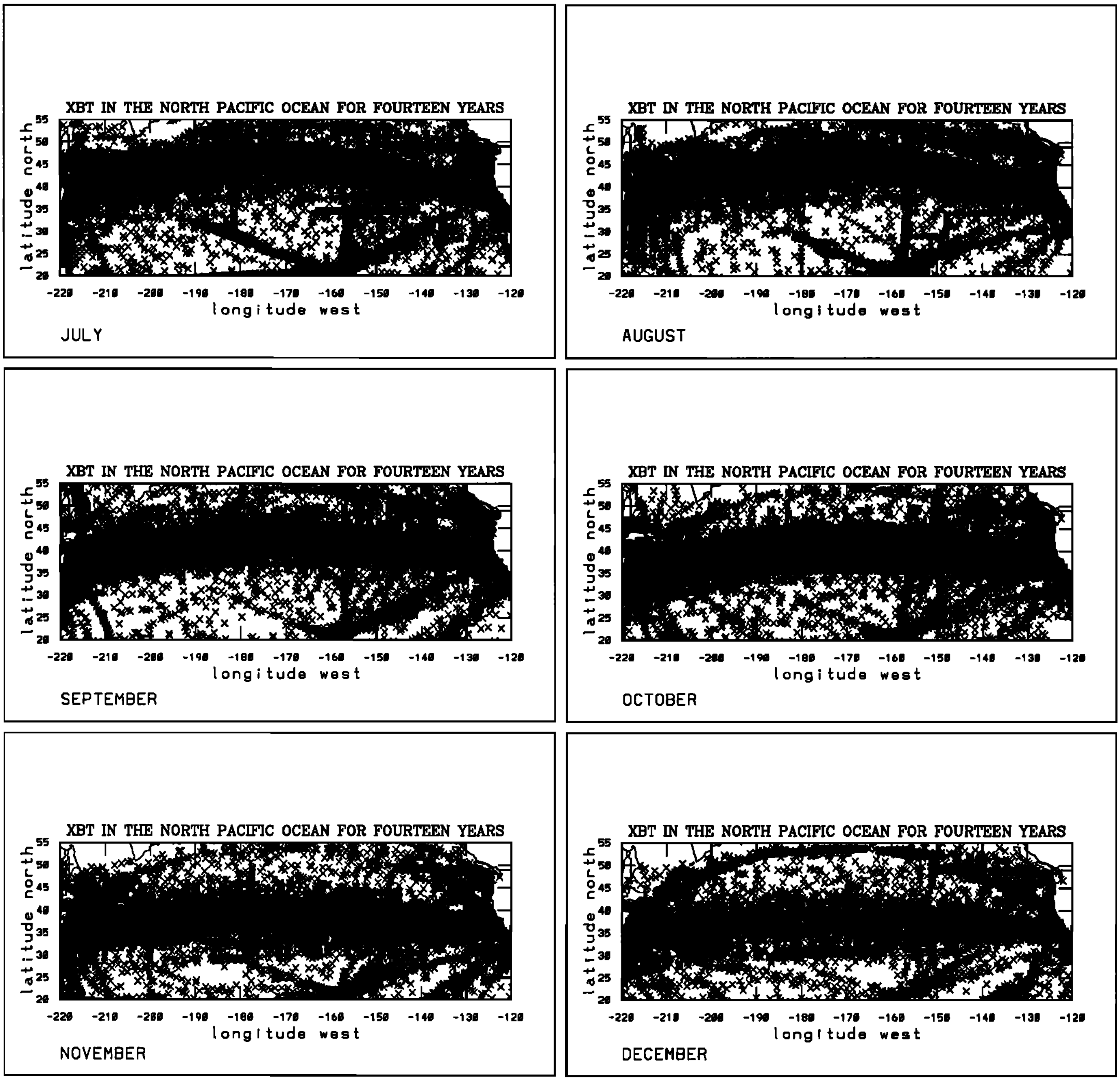

Fig. 1 (continued)

and depth values were recorded as positive real quantities to single decimal accuracy. The number of temperature values for a data point is not fixed, and the lowest depth to which temperatures are recorded is variable. The data points also have the year, month, date and hour recorded for the time that the record was taken. These parameters are recorded as integer variables in the data file. The total size of the data set exceeds 300 megabytes. The distributions of the XBT observations are shown in Figure 1. The XBT coverage tends to concentrate along the ship routes from the west coast of North America to Japan and from Hawaii to the west coast of North America. The density of observations during this period was highest in the middle latitudes.

In this study, the mixed layer depth was defined as the first depth at which the temperature was 0.1°C less than sea surface temperature. The temperature was first linearly interpolated into every meter for every individual profile, and then the mixed layer depth was computed by using the definition as mentioned above to obtain accuracy within one meter. In fact, in our XBT data analysis, the mixed layer depth patterns computed using 0.1° criterion are very similar to those using 0.2° or 0.5° criterion. We neglect salinity in diagnosing mixed layer depth because our model is only based on the three dimensional thermal energy conservation equation.

In order to remove the "bad" records, a simple statistical procedure was performed. The mixed layer depth values derived from individual temperature profiles were first av-

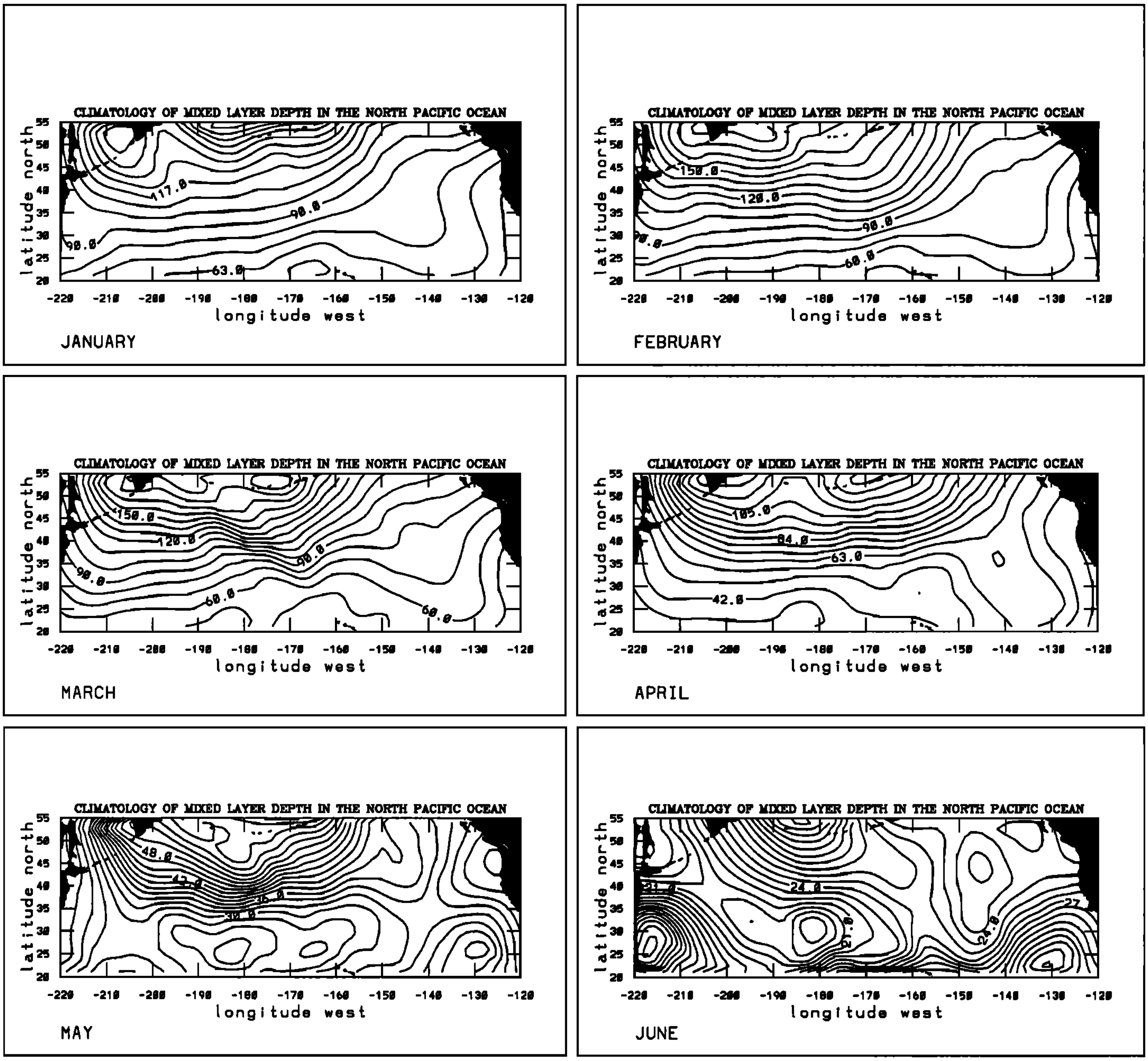

Fig. 2. Contour map of climatology of the monthly mean mixed layer depth (in meters) calculated from the XBT data set for the North Pacific Ocean.

eraged to a 2° latitude by 5° longitude grid by month, and then a biased sample variance was computed for every grid point. The individual mixed layer depth values beyond two estimated standard deviations were deleted. The cleaned-up mixed layer depth values were then again interpolated onto a 2° by 5° grid of latitude and longitude again by using a normal distribution weighting method. The method assured that the weight for every individual point to grid point was a normal distribution function of the distance between the individual point and grid point. Thus the weight of each individual mixed layer depth value point within a 2° latitude by 5° longitude grid to the grid point was defined as

$$f_i(x) = \frac{1}{\sqrt{2\pi}} e^{-\frac{x^2}{2}} \tag{30}$$

where x was the distance between the individual point and the grid point, $f_i(x)$ was the weight. The mixed layer depth value at each grid point was

$$MLD = \sum \frac{f_i(x)}{\sum f_i(x)} A_i \tag{31}$$

where A_i was the individual mixed layer depth value.

After this method was applied, the mixed layer depth value at each 2° by 5° grid point was obtained. Although the XBT data set for this study included more than 245,000 temperature profiles, it sometimes could not cover every grid point, and there were no data at some grid points during some months. The same interpolation method was used to fill in grid points where no data were available. The

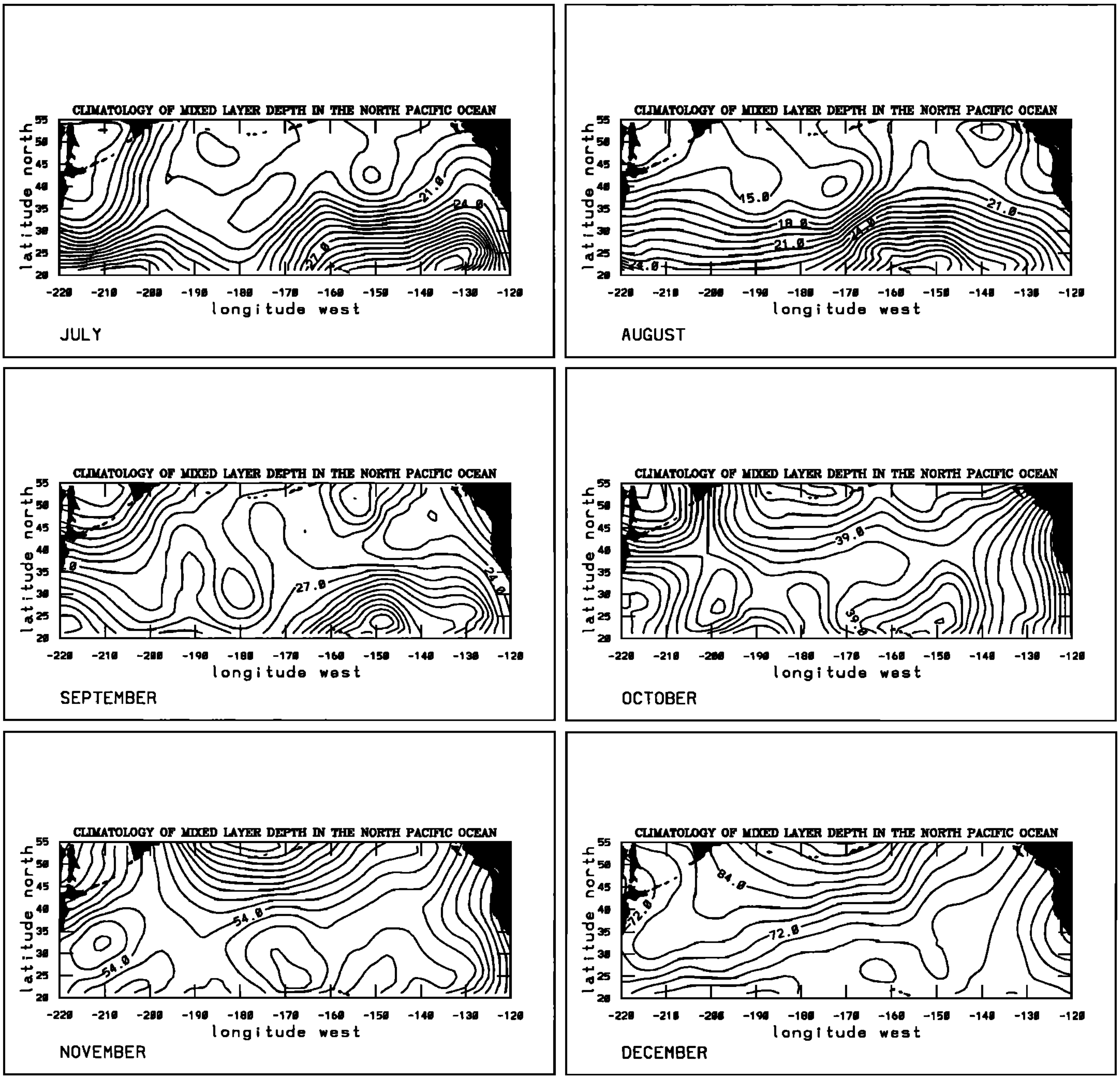

Fig. 2 (continued)

climatology of the monthly mean mixed layer depth was computed for the period 1976-1989 from this XBT data set. The results were plotted in Figure 2 and used as the sea truth data for comparison with model results.

Model Input Data

Satellite SST. MCSST data product derived from the TIROS- N/NOAA series AVHRR by Otis Brown, Rosenstiel School of Marine and Atmospheric Science (RSMAS), University of Miami, is distributed by Distributed Active Archive Center (DAAC), formerly the NASA Ocean Data System (NODS), at the Jet Propulsion Laboratory (JPL). This MCSST product consists of a weekly composite of data for the globe at approximately 18 km resolution as well as regional subsets. Presently, the JPL/DAAC has data from 1981 to 1991. In this study, the weekly MCSST data for the North Pacific Ocean from 1981 to 1991 were used to compute monthly mean SST and δSST, and to input into the model.

The TIROS-N/NOAA series polar orbiting satellites carried four-channel (TIROS-N, NOAA-6, NOAA-8, NOAA-10) or five-channel (NOAA-7, NOAA-9) AVHRR sensors as part of its payload. The primary objective of the AVHRR instrument is to provide cloud top and sea surface temperatures through passively measured visible, near-infrared, and thermal infrared spectral radiation bands. The AVHRR sensor has an instantaneous field of view (IFOV) that corresponds to a ground resolution of about 1.1 km at nadir, and

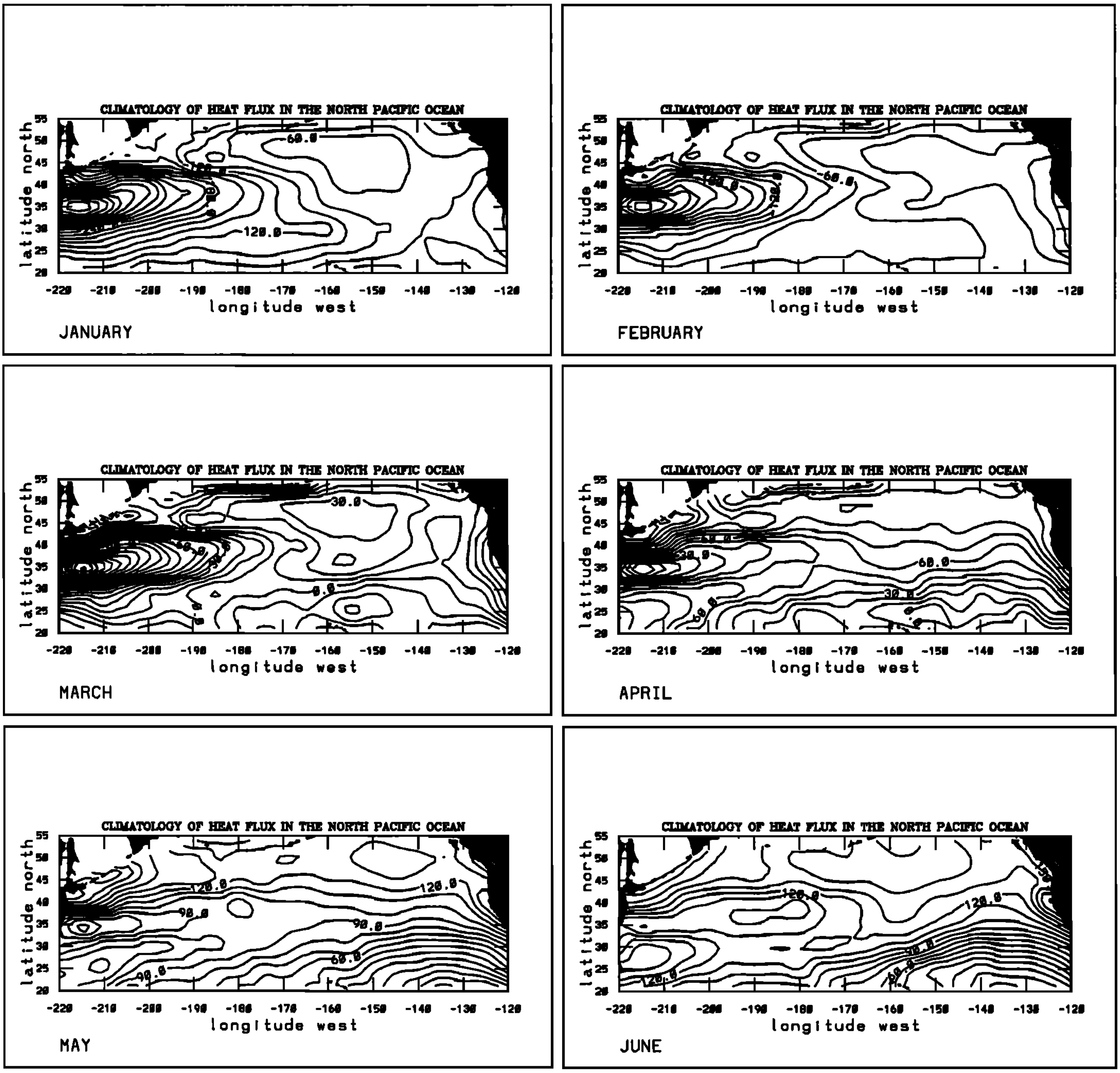

Fig. 3. COADS heat flux climatology (w/m^2).

a total scan field of view (FOV) of ± 55.4° from nadir (approximately 2240 km). The five spectral bands measured are channel 1, visible, 0.58-0.68 microns; channel 2, near-infrared, 0.725-1.10 microns; channel 3, infrared, 3.55-3.99 microns; channel 4, thermal infrared, 10.2-11.5 microns; and channel 5, a second thermal infrared channel at 11.5-12.5 microns (NOAA-7 and NOAA-9).

The MCSST product is derived from the NOAA/NESDIS Global Retrieval Tapes which contain MCSST retrievals with latitudes and longitudes. MCSST values are binned into a 2048 by 1024 pixel grid. For each grid point, the average of all MCSST measurements available for 1 week is computed. Open areas are interpolated using an iterative Laplacian relaxation technique until all such areas connected to valid observations are filled. A first guess for open areas is provided by computing the mean of horizontally bounding "good" data-filled pixels.

In this study, the weekly SST images were first averaged into monthly mean SST images. Plate 1 is an example of the monthly mean SST image for the North Pacific Ocean. Construction of δSST images was accomplished by subtracting, pixel by pixel, the registered SST image of the preceding month from the SST image of the following month. Plates 2a and 2b show the δSST images generated in this way for January and July 1989. In these δSST images, color scale represents the δSST in degrees Celsius. We can see that in summer, δSST is large and in winter, δSST is small or negative.

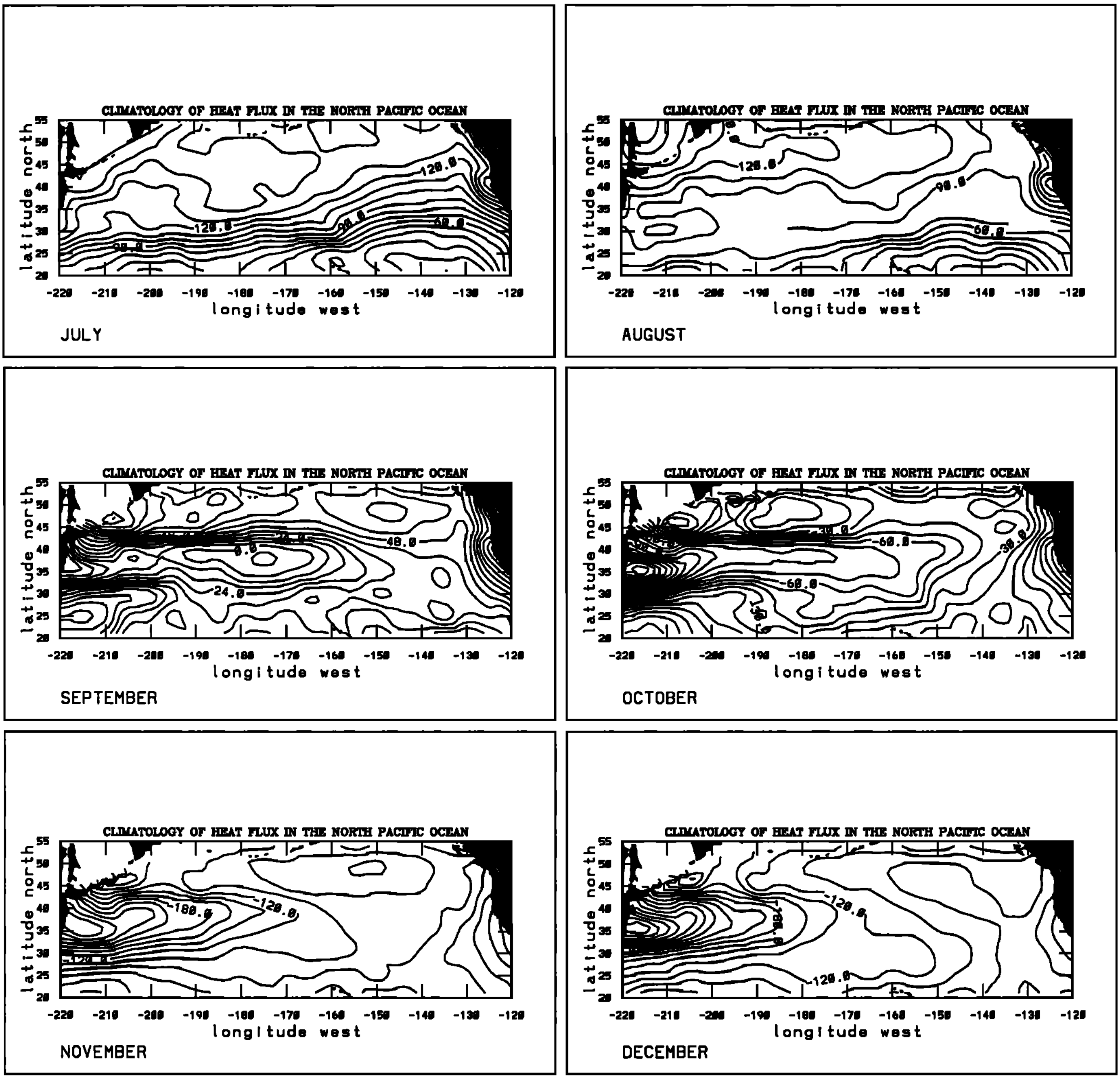

Fig. 3 (continued)

Heat flux and wind data. The heat flux data for this study were estimated by using bulk formulae parameterizations by *Cayan* [1990] from COADS, which were collected by merchant ships, meteorological buoys, and ocean weather ships. The COADS monthly mean data were first averaged to 2° latitude and longitude and then further averaged to a 5° by 5° grid to reduce the random error contained by this data. The data covered a period from January 1970 to December 1989, for the area from 20°N latitude to 55°N latitude and from 130°E to 110°W. The climatology has been computed for the period 1950-1989, and the monthly anomalies have been computed for the period 1910-1989.

There were two surface wind data sets available for this study. One was calculated from COADS, and the other was obtained from the Fleet Numerical Ocean Center (FNOC). The wind data of COADS was analyzed in the form of wind stress in units of m^2/s^2. In the same manner as for the COADS heat flux data, the COAD wind stress data were averaged onto a 5° latitude by 5° longitude grid, and the area covered was from 20°N latitude to 55°N latitude and from 130°E longitude to 110°W longitude. They were also averaged monthly. For the FNOC wind data set, it was in the form of wind stress in units of dynes/cm^2. The FNOC wind stress data set was in a daily form, covering the time period from January 1, 1975, to December 31, 1987. Figures 3 and 4 show the COADS heat flux climatology and wind speed climatology for the study areas.

Velocity fields. If we apply our 3-D thermal inertia model

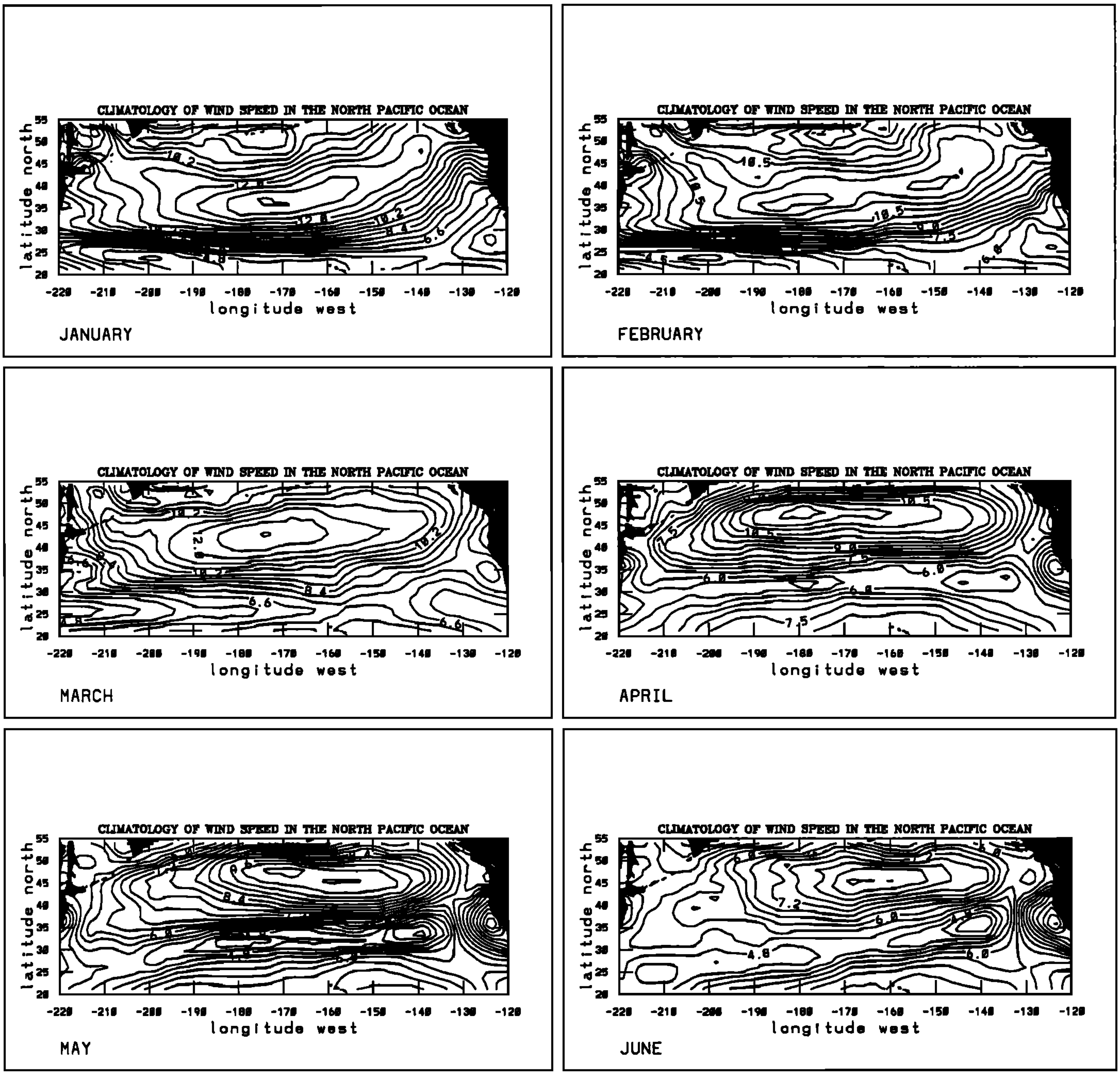

Fig. 4. COADS wind speed climatology (m/s).

to the small mesoscale oceanographic study and for the daily time scale, the velocity fields calculated from NOAA-AVHRR using a pattern recognition method developed by *Holland and Yan* [1991] could be used. In this study, the velocity fields we used as model inputs are obtained from Geosat altimetry (November 1986 to June 1989) and from VOS-XBT data (January 1976 to October 1986).

On November 8, 1986, the U.S. Navy's Geosat altimetric satellite was maneuvered into an orbit that repeats within 1 km every 17.0505 days, called the Exact Repeat Mission (Geosat ERM) and the resulting data were declassified and released. The NOAA's National Ocean Service used the low-level data from ERM to create two Geophysical Data Record (GDR) data sets, one for ocean heights and one for land and ice height [*Cheney et al.*, 1987, 1988]. These GDR's form the basis for much current work with Geosat. Our source data are the GDR's processed by NOAA, which have been corrected for atmospheric influences (wet and dry tropospheric plus ionospheric corrections), tides, sea state bias, and inverse barometer effect. Further processing includes geoid error reduction for each track by subtracting a reference elevation profile along the track from all of the elevation profiles measured along the track [*Halpern et al.*, 1991]. The orbit error, which is typically the largest after all corrections have been made, has been further reduced to about 5 cm rms by fitting and removing a once-per-revolution sine wave [*Halpern et al.*, 1991]. The resulting Sea Surface Elevation (SSE) data have been used for calculating the ocean

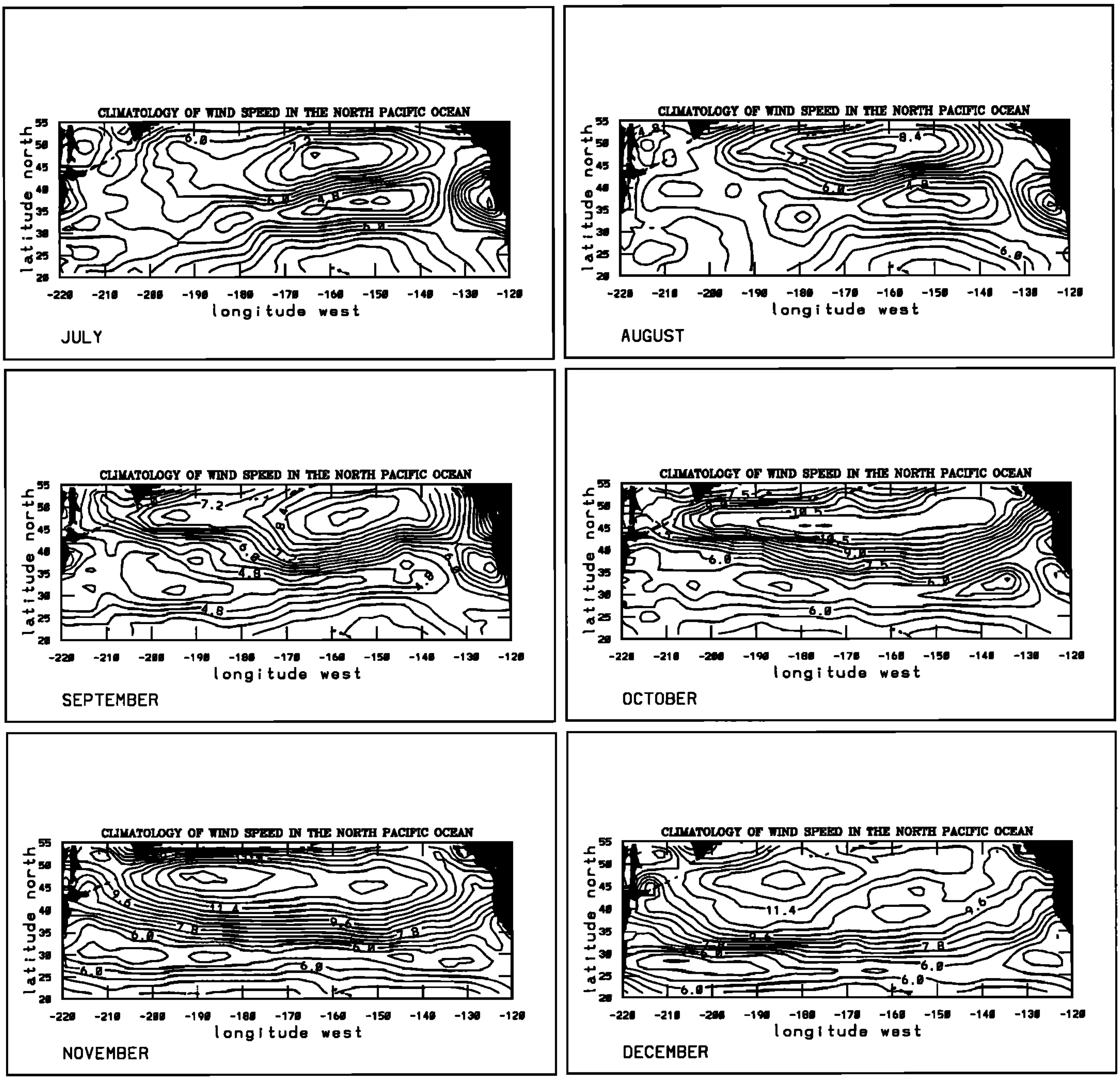

Fig. 4 (continued)

surface velocity by using a simple geostrophic equilibrium equation. Horizontal velocity field is obtained from a balance between the Coriolis force and the pressure gradient [*Wunsch and Gaposchkin*, 1980]:

$$V - V_r = \frac{g}{\rho f} \int_{z_r}^{\eta} \frac{\partial \rho}{\partial h} dz \tag{32}$$

where V is surface velocity, V_r is reference velocity, ρ is density, g is acceleration of gravity, f is Coriolis parameter, h is horizontal coordinate, z_r is reference level, and η is surface elevation.

If we choose the geoid as the reference level, the surface velocity is determined by the surface elevation gradient:

$$V_x = \frac{g}{f} \cdot \frac{\partial \eta}{\partial x} \tag{33}$$

$$V_y = \frac{g}{f} \cdot \frac{\partial \eta}{\partial y} \tag{34}$$

$$V = \sqrt{V_x^2 + V_y^2} \tag{35}$$

VOS-XBT data, along with the *Levitus* [1982] atlas-analyzed fields, have been used to create density and geostrophic velocity for 1976-1986. For XBT data, linear relationships between temperature and salinity obtained from *Emery* [1983] have been used to estimate density from tem-

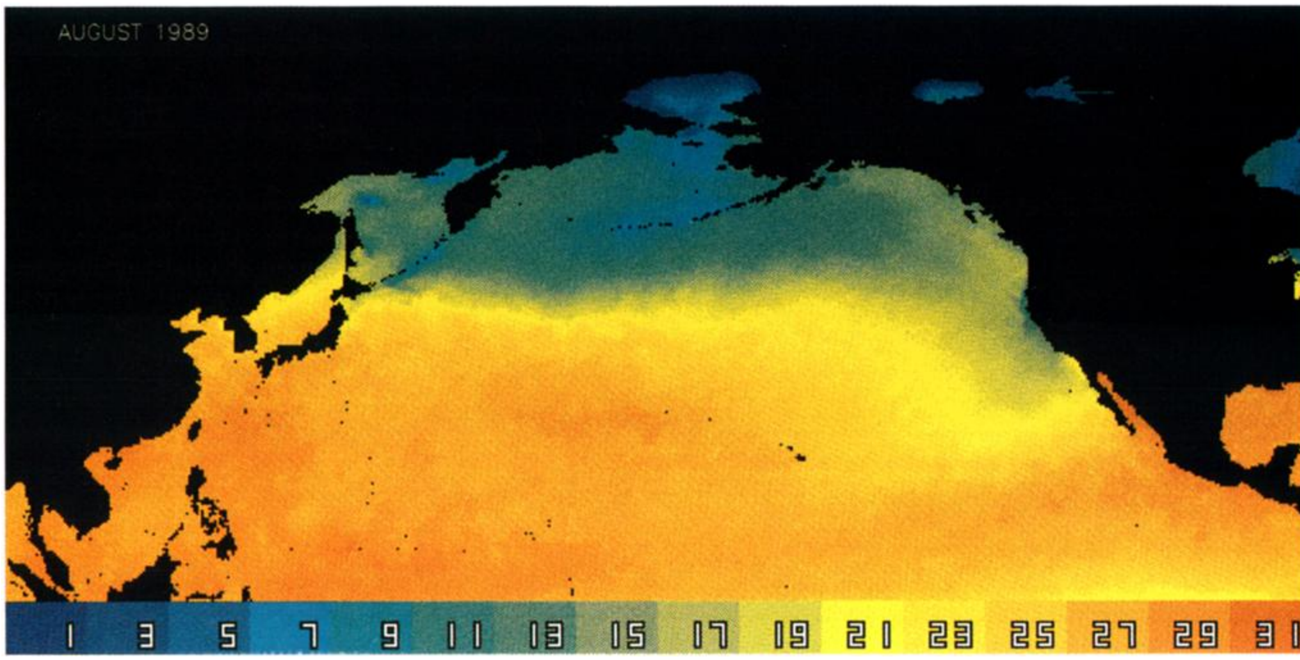

Plate 1. Monthly mean SST image (August 1989) calculated from AVHRR-MCSST data provided by PODAAC at JPL.

perature alone. Geostrophic velocity cross sections have then been calculated from the density cross sections in each longitude and latitude band and used in the model as an alternative to Geosat altimeter data.

In this study, we also estimate the wind-driven advection using wind data we possessed and incorporate it into the model for advection. The vertical velocity w then can be calculated from u and v, using the equation of continuity, i.e. $\partial w/\partial z = -(\partial u/\partial x + \partial v/\partial y)$. Assuming $w = 0$ at $z = 0$, the velocity at depth D is given by

$$w_D = -\int_0^D \left(\frac{\partial u}{\partial x} + \frac{\partial v}{\partial y}\right) dz$$

We use this vertical velocity as a typical value for w in our model.

APPLICATION OF THE MODEL

The model was tested for the period of 1981-1989 using NOAA-AVHRR MCSST data, altimeter data, COADS, and VOS-XBT data based on the methods discussed in the previous sections and in *Yan et al.* [1991*a*]. Briefly, mixed layer depth images are produced as follows: monthly mean sea surface temperature images are made from thermal infrared radiance data acquired by the NOAA-AVHRR sensor. The data are rectified to account for such systematic effects as instrument optics, viewing geometry, and platform motion.

The images and other data mentioned in previous sections are registered to a standard grid. Then an SST difference (δSST) image is formed by subtracting the registered SST image of the preceding month from the SST image of the following month, on a pixel by pixel basis. The model is run repeatedly to generate a look-up table of thermal inertia values as a function of sea surface temperature change, flux, wind, and surface current magnitude. To produce a thermal inertia fields, each grid is assigned a thermal inertia value from the model based on δSST, flux, wind, and current magnitude for that grid. Finally, the thermal inertia is converted to the mixed layer depth through a linear regression equation obtained from data. As an example, Plate 3 shows the model-simulated mixed layer depth for the North Pacific Ocean for February, and this can be compared with sea truth data–climatology of the mixed layer depth calculated from 14 years of XBT data (Plate 4). Plates 5 and 6 are similar comparisons for the August mixed layer depth in the North Pacific Ocean. In order to see the three-dimensional feature more clearly, we turned the conventional coordinates upside down, that is, the top is towards the south. Figures 5 and 6 are time series comparisons of zonally averaged mixed layer depths generated by the model (dashed line) and zonally averaged mixed layer depths calculated from VOS-XBT observations (solid line) for 25°N and 45°N in Pacific Ocean. We can see clearly from Plates 3–6 and Figures 5 and 6 that the predicted mixed layer depths agree well with those observed from VOS-XBT data.

From the model results and the VOS-XBT data, we can see that the deepest mixed layer depth value was about 210 m and was found at the Bering Sea in February. The shallowest mixed layer depth value was around 15 m and was obtained in the central North Pacific Ocean in August. The mixed layer depth varied from 60 m to 210 m in winter and from 15 to 30 m in summer. From January to May, the mixed layer depth was deeper in the higher latitudes (e.g., Plate 3). In June, the shallowest mixed layer depth was around middle latitudes. From July to October, the mixed layer depth was deeper in the low latitudes (e.g., Plate 5). From November to December, the mixed layer depth was again deeper in the higher latitudes. The smooth mixed layer depth gradients along latitudes appeared from January to April. Some mesoscale features appeared and were travelling northward from May to August. An interesting phenomenon found in the mixed layer topography was that

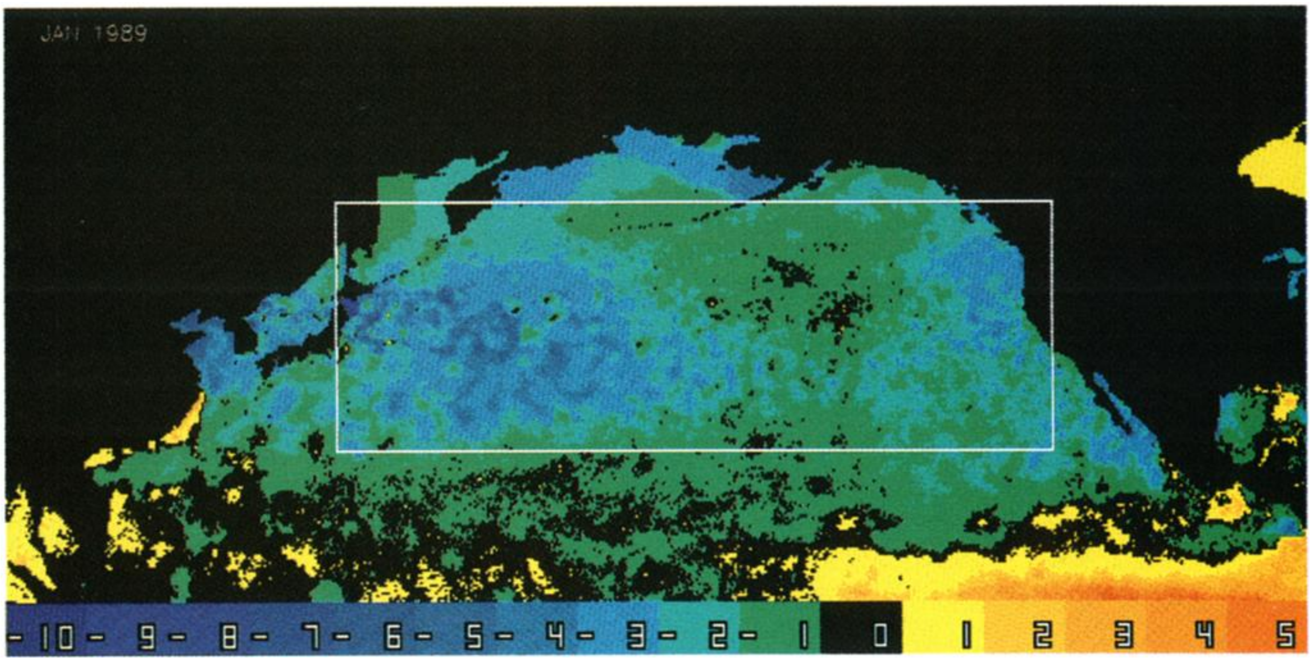

Plate 2*a*. The δSST image for January 1989.

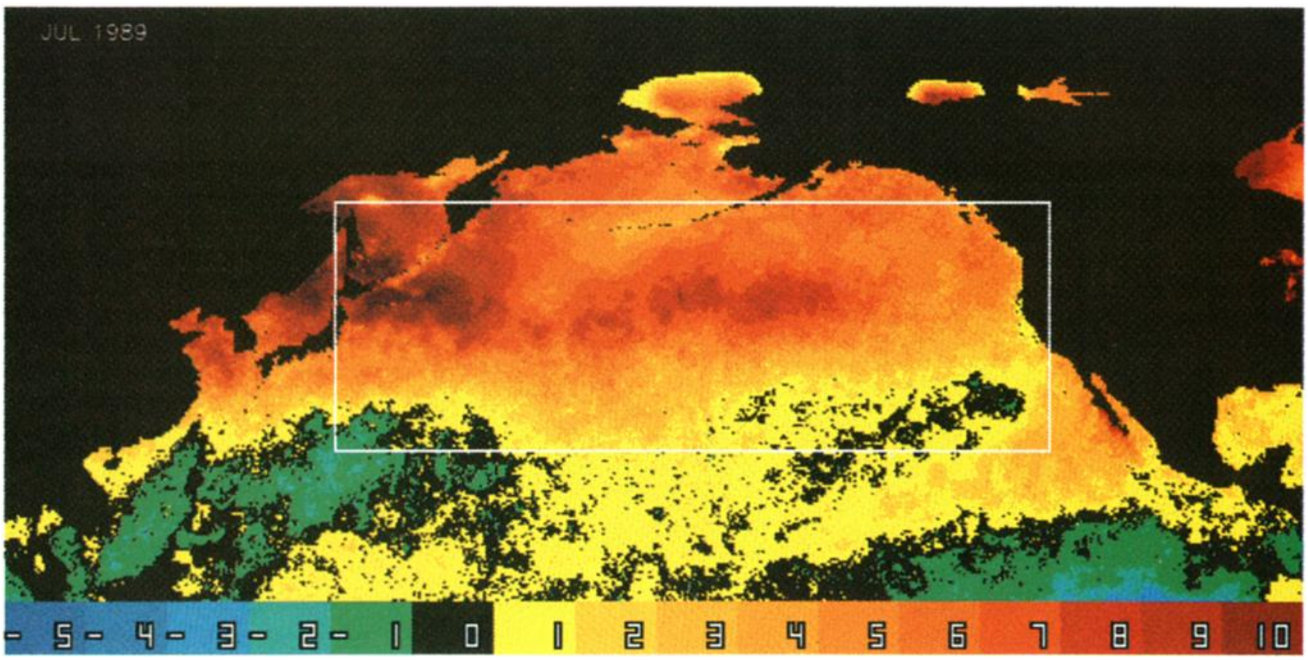

Plate 2*b*. The δSST image for July 1989.

the mixed layer depth gradient was larger at the northwest of the North Pacific Ocean than that at the other regions in winter, while, from June to October, the larger gradient appeared at the southeast of the North Pacific Ocean. This implied that the mixed layer depth variability was larger in the northwest of the North Pacific Ocean than that in the other regions in winter, while, in summer, the large mixed layer depth variability was found in the southeast of the North Pacific Ocean.

The correlation coefficients between the zonally averaged mixed layer depth and the zonally averaged δSST are shown in Table 1 for each 5° latitude for the whole 9 years (1981–1989). The period June to November represents the summer part of the year, and the period December to May represents the winter part of the year. We can see that the correlation coefficients between the mixed layer depth and δSST computed from cleaned data were higher than those computed from raw data. The magnitude of the correlation coefficients was more than 0.65 at every 5° latitude in the summer, but this happened only at lower latitudes in the winter. Since wind speed was strong at higher latitudes in the winter, it could be that the relative low correlation between the mixed layer depth and δSST was caused by the influence of wind generated vertical entrainment increases. Thus the corre-

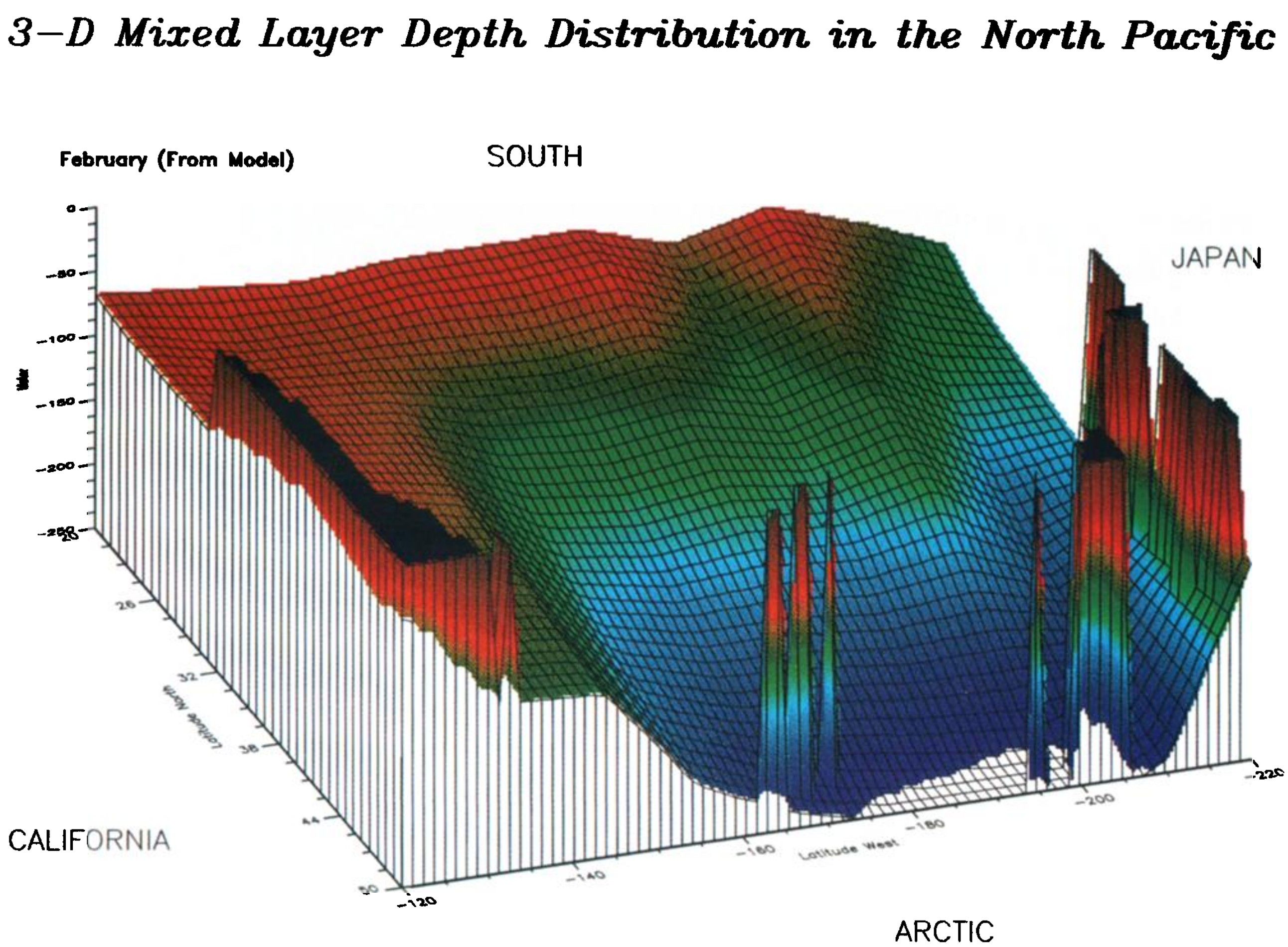

Plate 3. Three-dimensional (3-D) display of the climatology of the mixed layer depth for the North Pacific Ocean for February calculated from 3-D thermal inertia model. Top is toward south.

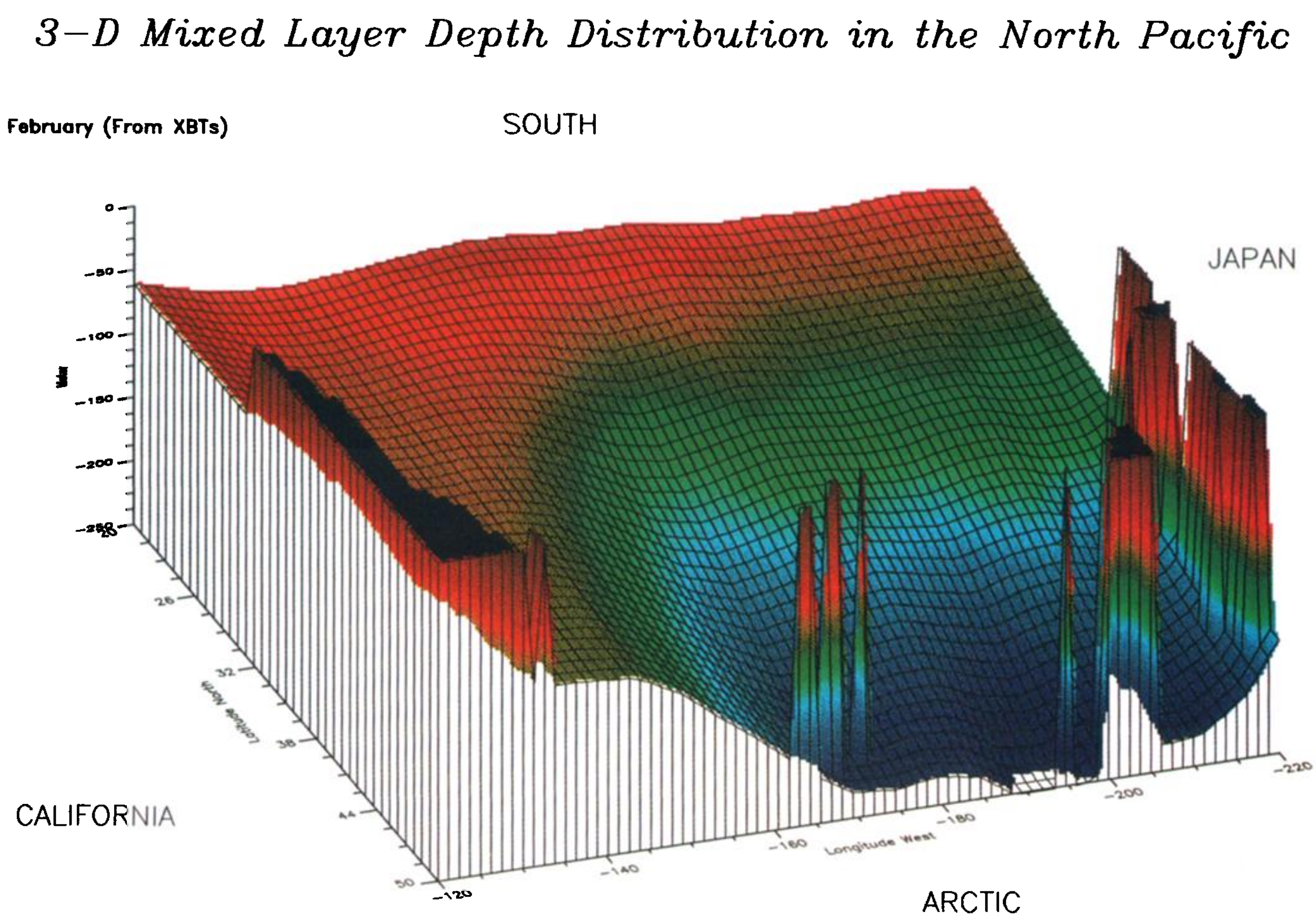

Plate 4. Climatology of the mixed layer depth for February calculated from VOS-XBT data. Top is toward south.

3–D Mixed Layer Depth Distribution in the North Pacific

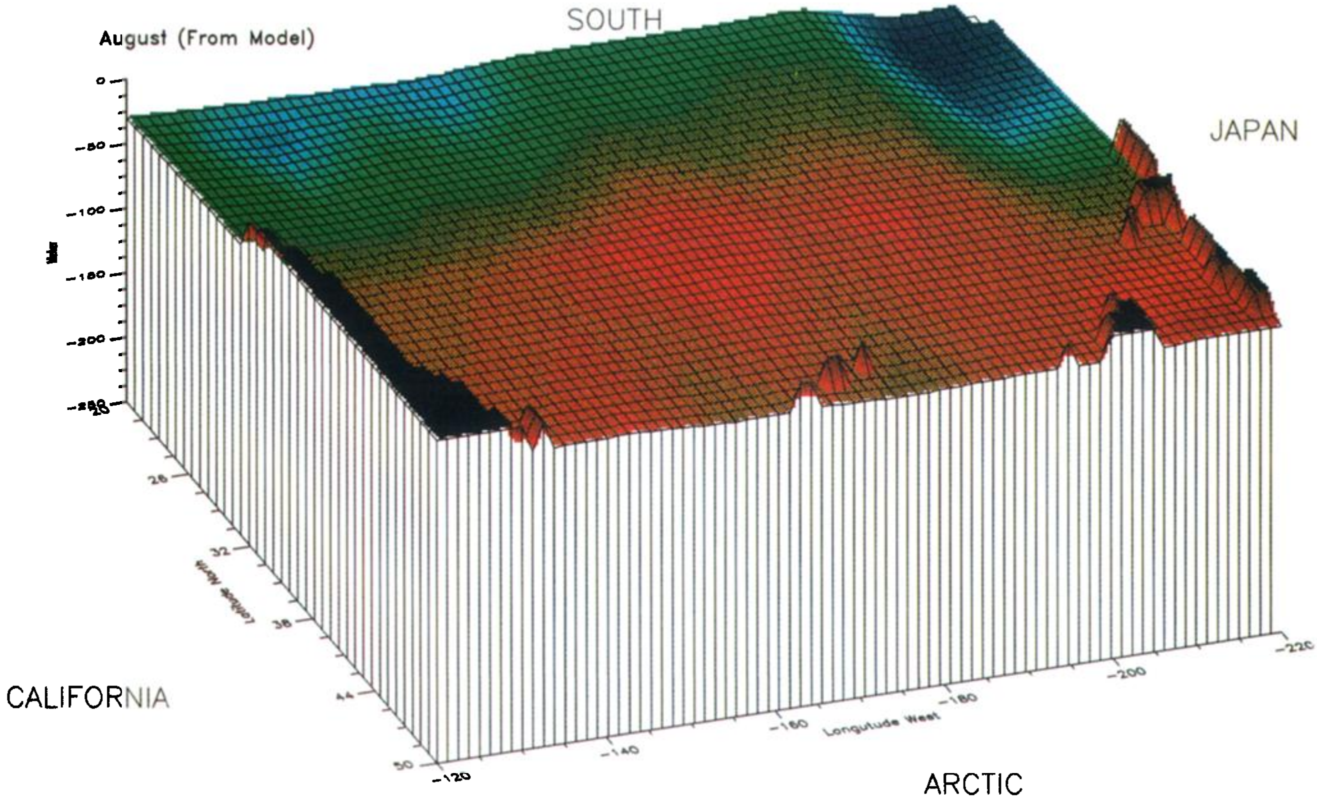

Plate 5. Three-dimensional (3-D) display of the climatology of the mixed layer depth for August calculated from the 3-D thermal inertia model. Top is toward south.

3–D Mixed Layer Depth Distribution in the North Pacific

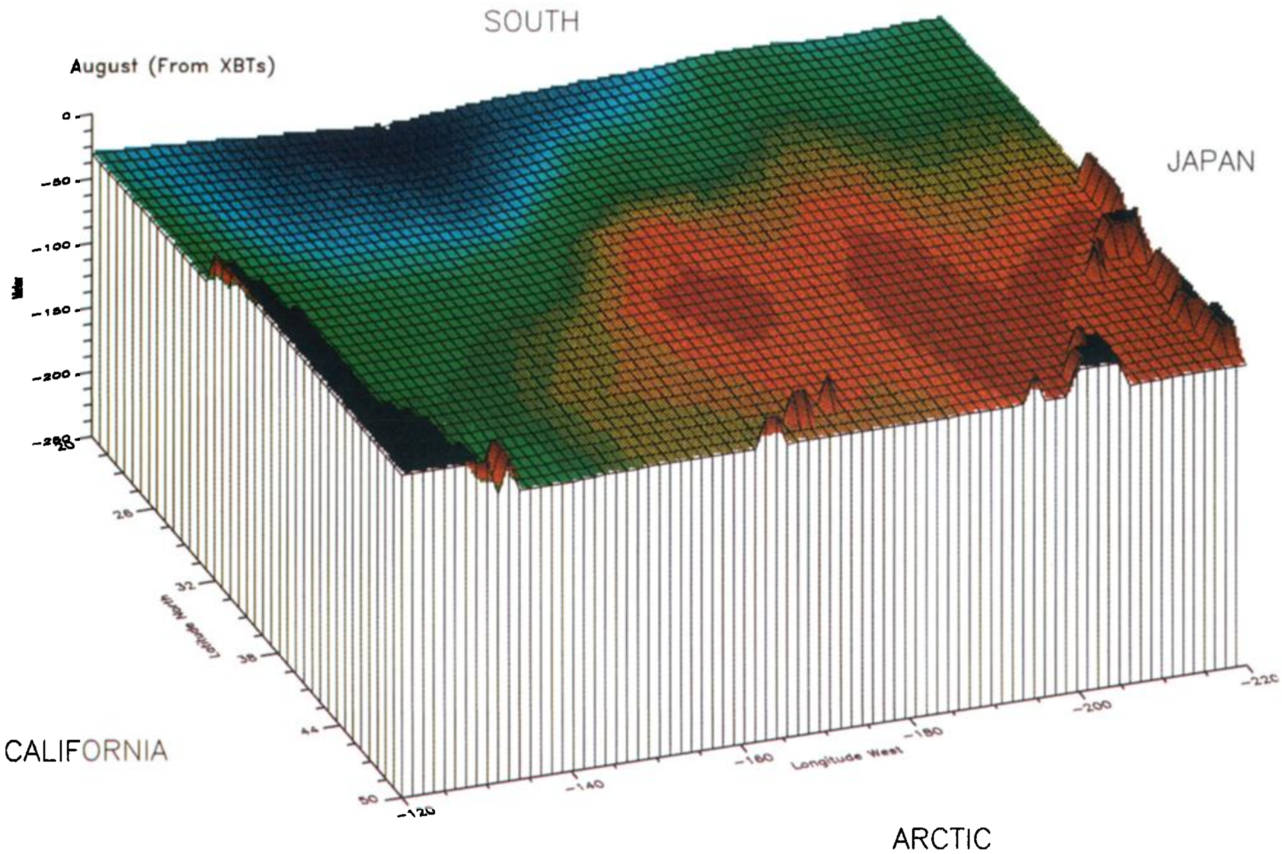

Plate 6. Climatology of the mixed layer depth for August calculated from VOS-XBT data. Top is toward south.

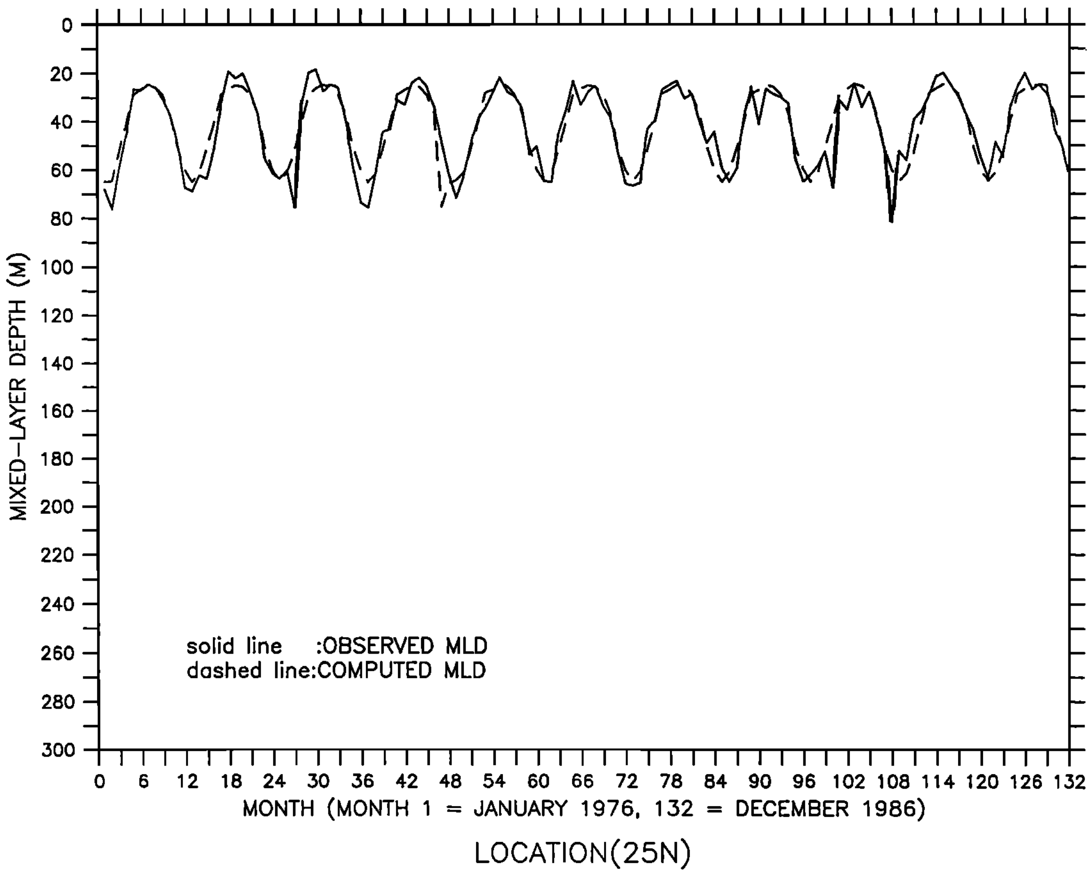

Fig. 5. Time series comparisons of observed zonally averaged mixed layer depth (25°N) and model-computed zonally averaged mixed layer depth.

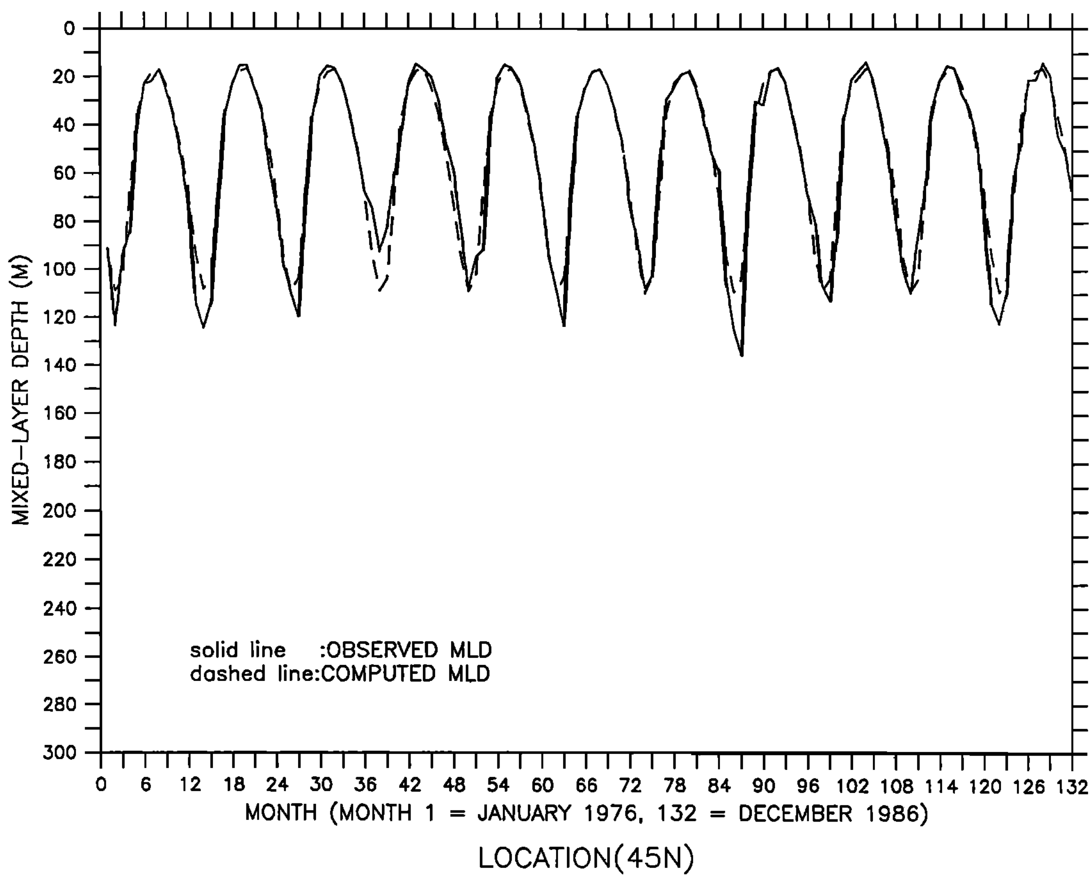

Fig. 6. Time series comparisons of observed zonally averaged mixed layer depth (45°N) and model-computed zonally averaged mixed layer depth.

TABLE 1. Correlation Coefficients Between the Zonally Averaged Mixed Layer Depth and the Zonally Averaged δSST

	Year		June–Nov.		Dec.–May	
Latitude	Raw Data	Clean Data	Raw Data	Clean Data	Raw Data	Clean Data
55	-0.26	-0.29	-0.60	-0.56	-0.33	-0.36
50	-0.29	-0.43	-0.66	-0.60	-0.32	-0.50
45	-0.42	-0.44	-0.71	-0.68	-0.42	-0.49
40	-0.51	-0.54	-0.67	-0.70	-0.51	-0.61
35	-0.55	-0.56	-0.75	-0.75	-0.63	-0.68
30	-0.57	-0.57	-0.76	-0.77	-0.70	-0.75
25	-0.57	-0.57	-0.66	-0.81	-0.67	-0.67
20	-0.55	-0.33	-0.56	-0.78	-0.68	-0.48

lation results implied that the mixed layer depth may be influenced by wind more than by heat flux at higher latitudes in the winter.

The time series of the modeled zonally averaged mixed layer depth versus the zonally averaged δSST calculated from AVHRR-MCSST data is shown in Figure 7. A positive (or larger) δSST implies that the sea surface for the following month was warmer than that for the previous month, while a negative δSST implies that the sea surface for following month was cooler than that for previous month. It was very clear that the mixed layer depth was strongly influenced by the warming and cooling mechanism. For example, the larger δSST indicated the shallower mixed layer depth, while the smaller δSST (including negative δSST) indicated the deeper mixed layer depth. Similarly the vertical entrainment effects were accounted for by changes of δSST. For example, if vertical entrainment was larger, the mixed layer depth would be deeper and δSST would be smaller or negative, and vice versa. These phenomena are consistent to the thermal inertia concept and the relationship among the thermal inertia, the sea surface temperature changes (δSST), and the mixed layer depth described by *Yan et al.* [1990*a*].

From Figure 7, we can also see clearly that the mixed layer depth lagged δSST by some months. To investigate

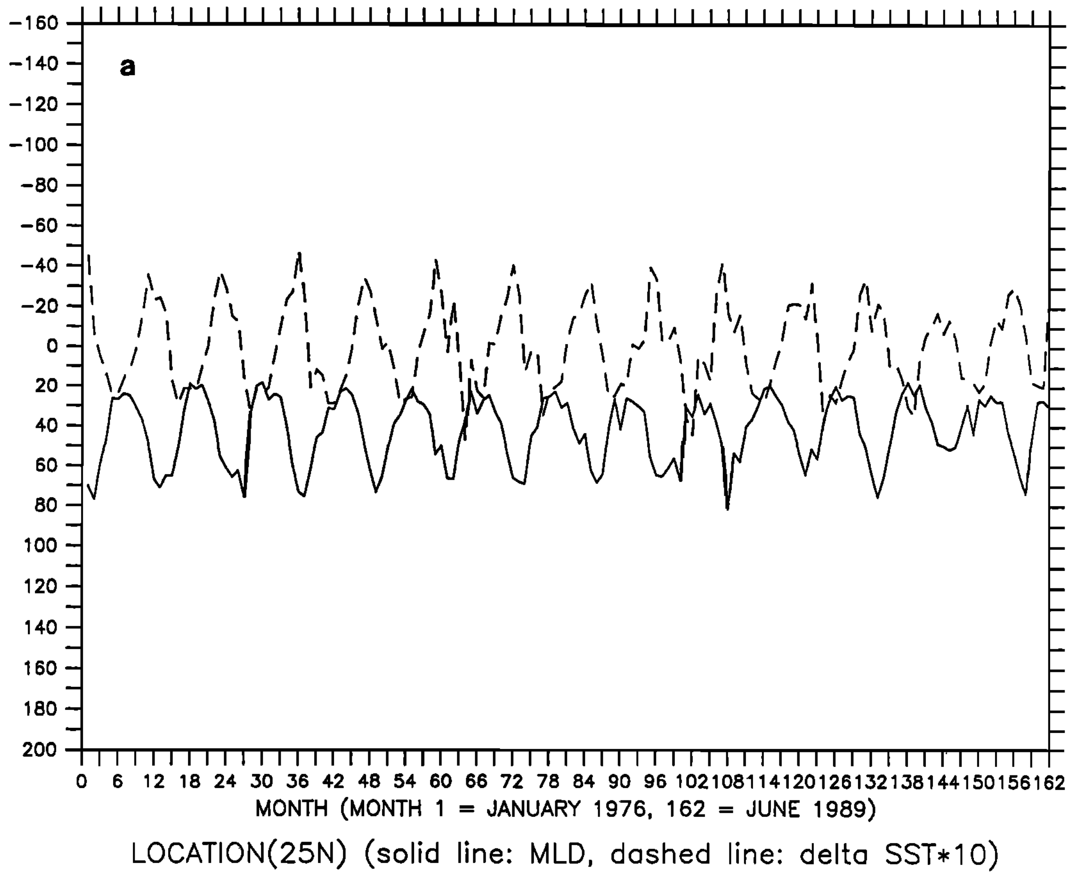

Fig. 7. Time series of the modeled zonally averaged mixed layer depth versus the zonally averaged δSST calculated from AVHRR-MCSST data. The solid line is the mixed layer depth. The dashed line is δSST scaled up by a factor of 10. Comparison at (a) 25°N, (b) 35°N, and (c) 45°N.

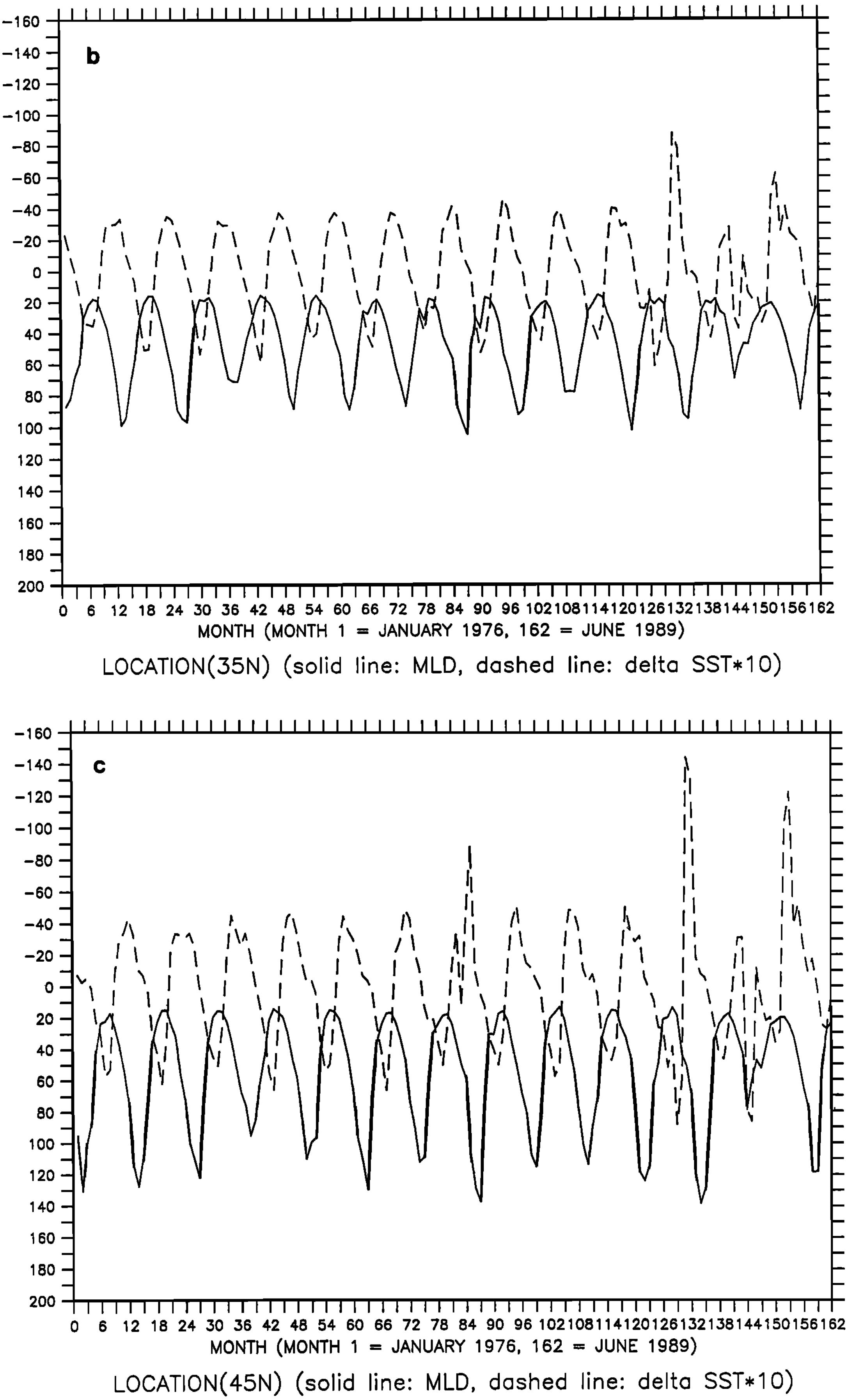

Fig. 7 (continued)

TABLE 2. Correlation Coefficients Between the Mixed Layer Depth (Lags δSST) and δSST

Latitude	phase lag 0 month	1 month	2 months	3 months
55	-0.29	-0.54	-0.66	-0.68
50	-0.43	-0.57	-0.69	-0.69
45	-0.44	-0.67	-0.76	-0.67
40	-0.54	-0.76	-0.80	-0.66
35	-0.56	-0.80	-0.85	-0.68
30	-0.57	-0.83	-0.87	-0.69
25	-0.57	-0.85	-0.81	-0.57
20	-0.33	-0.67	-0.70	-0.50

the phase lag of the mixed layer depth to δSST, correlations were computed using 1-month, 2-month, and 3-month lags, respectively, and are tabulated in Table 2. At 55°N latitude, the highest correlation calculated was for a phase lag of 3 months; at middle latitudes (30°-55° N), for a lag of 2 months, and in the subtropics (20°-25° N), for a lag of 1 month. It seemed that the phase lag increased with latitude.

The correlation coefficients between the mixed layer depth anomaly and the heat flux anomaly were mapped for the North Pacific Ocean at each grid point for every month and are plotted in Figure 8. The correlation coefficients greater than 0.5 were found offshore of the California coast during December, January, March, and from June to July. We also found that higher correlation occurred in the Central North Pacific Ocean during most months. The correlation coefficients between the mixed layer anomaly and wind speed anomaly for North Pacific Ocean were also computed and plotted (Figure 9). Similar to the heat flux anomaly correlation analysis results, the higher correlation coefficients appeared more frequently in the central North Pacific Ocean than in the other regions. Figures 8 and 9 implied that the mixed layer depth topography in the North Pacific Ocean depends on both local forcings and large scale circulation. The mixed layer depth in the central North Pacific Ocean

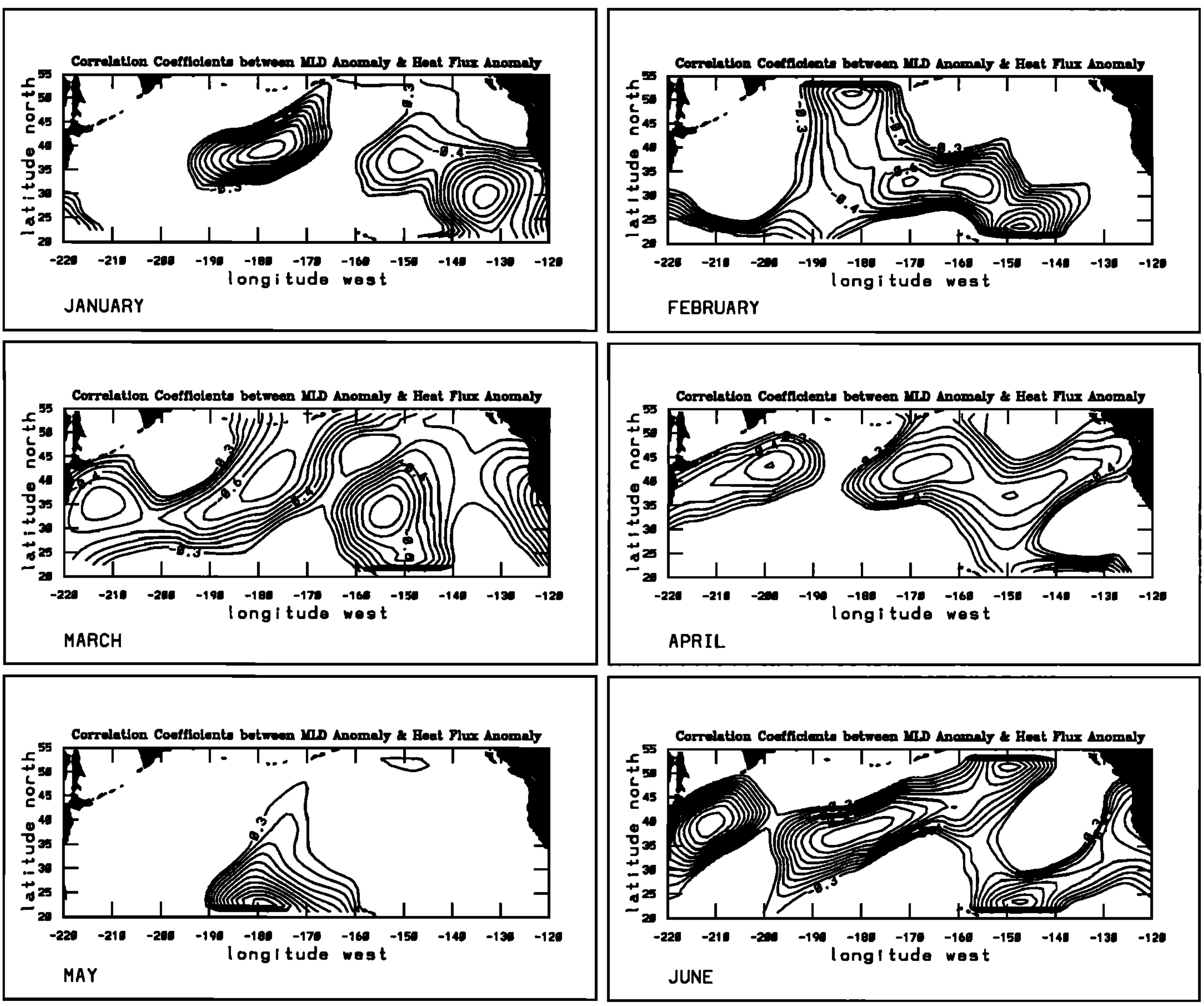

Fig. 8. Correlation coefficients (CC) between the mixed layer depth anomaly and the heat flux anomaly. Only those CC's greater than 0.3 are plotted.

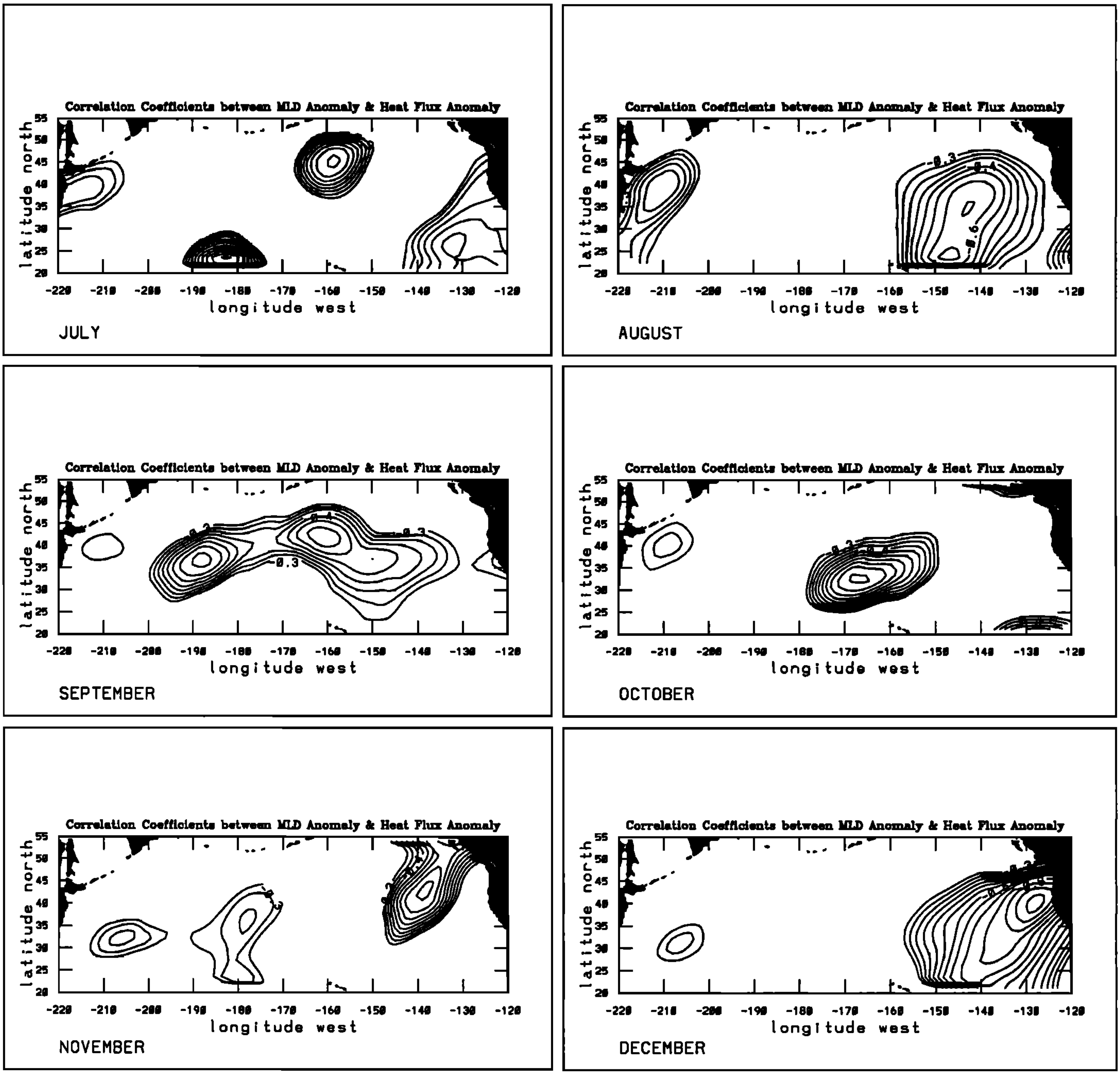

Fig. 8 (continued)

seems to be controlled to a large extent by local atmospheric forcings, while in the major current systems, variations in the thermal structure in the upper layer due to horizontal advection are large, and the simulation of the mixed layer depth is much more complicated. A three-dimensional approach is really necessary.

DISCUSSION AND CONCLUSION

Our present understanding of ocean general circulation is based upon a rather crude representation of the surface mixed layer. Although simplifications regarding mixed layer physics have provided analytical insight into the large-meso scale circulation, explicit representation of the mixed layer is essential if we are to go beyond this basic understanding.

Up to now, not much detailed understanding is available on the large-scale mixed layer depth because of the harshness of the marine environment. No single variable that can be observed globally is a reliable indicator of global mixed layer depth. For example, conventional wisdom dictates that decreasing SST is related to increasing mixed layer depth [*Halpern*, 1974; *Davis et al.*, 1981]. However, this correlation is poor in regions where advection contributes significantly to mixed layer depth variations, as in the equatorial region [*Halpern*, 1987] and in the regions of major current systems in the North Pacific Ocean [*Yan et al.*, 1990*b*].

Satellite observations have added a new dimension to the process of describing the ocean. While satellite observations give information primarily about the surface layer of

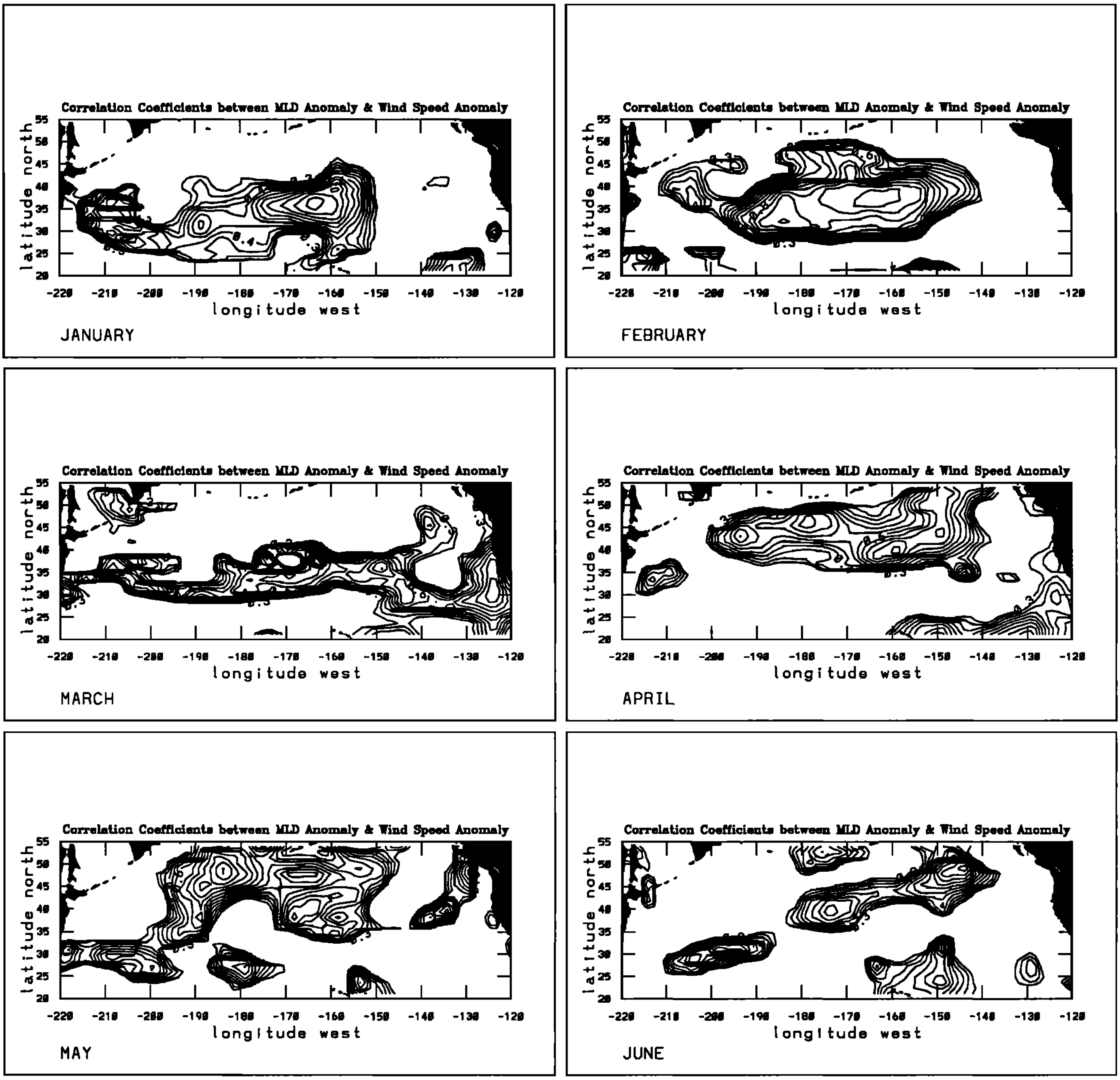

Fig. 9. Correlation coefficients between the mixed layer depth anomaly and the wind speed anomaly. Only those CC's greater than 0.3 are plotted.

the oceans, their synoptic coverage often gives vital information that is difficult, or impossible, to obtain from any other method. *Yan et al.* [1990*a*, 1991*b*] described an one-dimensional thermal inertia mixed layer model to estimate the daily mean mixed layer depth using satellite data. The limitation of that model is that it only works well in the regions where advection and horizontal diffusion are small.

In this study we developed a three-dimensional semi-analytical thermal inertia mixed layer model which includes the advection terms and the horizontal diffusion terms in our previous model. The model was tested using the data from AVHRR-MCSST data set, Geosat Altimeter data set, and from the COADS data set for the North Pacific Ocean. The model predicted mixed layer depths were compared favorably with the mixed layer depths calculated from 14 years of VOS-XBT data set. The results of this study also demonstrate that the mixed layer depth in the central North Pacific Ocean seems to be controlled to a large extent by local atmospheric forcings, while in the major current systems, such as Kuroshio and California current, variations in the thermal structure in the upper ocean due to horizontal advection are large, and a three dimensional approach is really necessary in the simulation of the mixed layer processes.

Additional improvements in the future in mixed layer depth mapping may be provided by incorporating digital heat flux data and wind data from new and on-going satel-

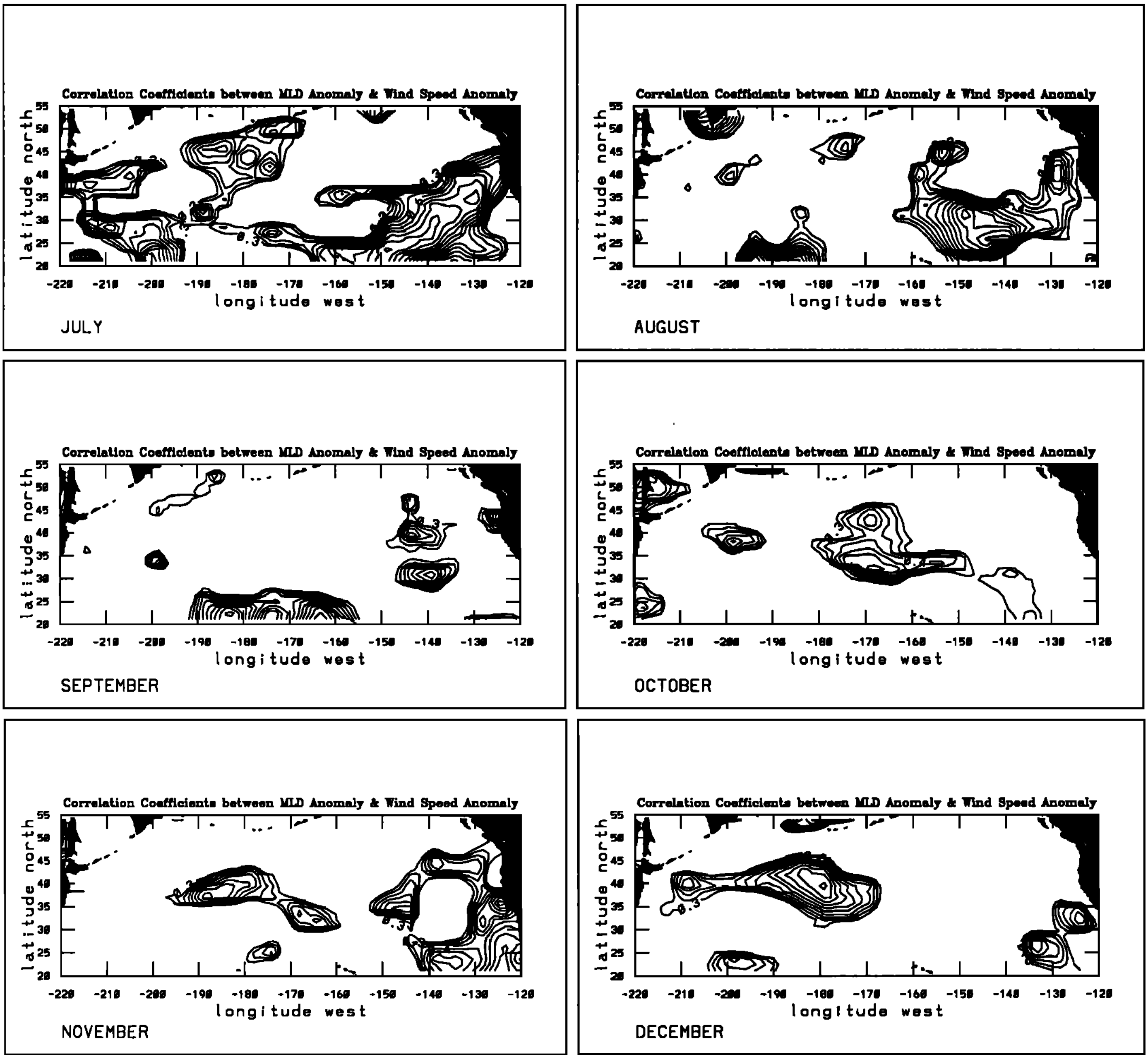

Fig. 9 (continued)

lite systems into the model. Wind velocity can be calculated from the European Space Agency (ESA) ERS-1 and ERS-2 spacecrafts' AMI data. ERS-1 was launched in July 1991 and has an anticipated lifetime of about 2 years. ERS-2, identically equipped, is proposed to overlap at the end of ERS-1 lifetime. The AMI on ERS-1 and ERS-2 could measure surface wind vectors at C-band when put in scatterometer mode. Additionally, insolation and cloud cover, latent heat flux, and outgoing long-wave radiation can all be calculated using measurements made from space. Latent heat flux can be calculated from SSM/I, one of the microwave instruments carried by the Defense Meteorology Satellite Program (DMSP) spacecraft, and insolation can be derived from both NOAA Polar-Orbiting meteorological satellites and the GMS satellite [*Liu*, 1988]. Therefore, we believe that our remote sensing mixed layer models are potentially useful tools to predict both daily and monthly mixed layer depth and that they might be applied to operational upper ocean forecasting when the real time satellite observations required by models are available. This application will certainly allow a better understanding of air-sea interaction, upper ocean response, and mixed layer dynamics, and it will be important to global change studies.

APPENDIX: ANALYTICAL SOLUTION FOR EQUATION (1′)

The transformation

$$T(x,y,z,t) = C(x,y,z,t)\ \exp\left[\left(\frac{u}{2K_x}x - \frac{u^2}{4K_x}t\right) + \left(\frac{v}{2K_y}y - \frac{v^2}{4K_y}t\right) + \left(\frac{w}{2K_z}z - \frac{w^2}{4K_z}t\right)\right] \qquad \text{(A1)}$$

makes (1′) a simpler form:

$$\frac{\partial C}{\partial t} = K_x \frac{\partial^2 C}{\partial x^2} + K_y \frac{\partial^2 C}{\partial y^2} + K_z \frac{\partial^2 C}{\partial z^2} \tag{A2}$$

which is subject to

At $t = 0$

$$C = C_0(x,y,z) = T_0(x,y,z) e^{-\frac{u}{2K_x}x - \frac{v}{2K_y}y - \frac{w}{2K_z}z}. \tag{A3}$$

At $x = 0$

$$C = T_{11}(y,z,t) e^{-\frac{v}{2K_y}y - \frac{w}{2K_z}z} e^{\left(\frac{u^2}{4K_x} + \frac{v^2}{4K_y} + \frac{w^2}{4K_z}\right)t}$$

$$\equiv C_{11}(y,z,t). \tag{A4}$$

At $x = L_x$

$$C = T_{12}(y,z,t) e^{-\frac{v}{2K_y}y - \frac{w}{2K_z}z - \frac{u}{2K_x}L_x} e^{\left(\frac{u^2}{4K_x} + \frac{v^2}{4K_y} + \frac{w^2}{4K_z}\right)t}$$

$$\equiv C_{12}(y,z,t). \tag{A5}$$

At $y = 0$

$$C = T_{21}(x,z,t) e^{-\frac{u}{2K_x}x - \frac{w}{2K_z}z} e^{\left(\frac{u^2}{4K_x} + \frac{v^2}{4K_y} + \frac{w^2}{4K_z}\right)t}$$

$$\equiv C_{21}(x,z,t). \tag{A6}$$

At $y = L_y$

$$C = T_{22}(x,z,t) e^{-\frac{u}{2K_x}x - \frac{w}{2K_z}z - \frac{v}{2K_y}L_y} e^{\left(\frac{u^2}{4K_x} + \frac{v^2}{4K_y} + \frac{w^2}{4K_z}\right)t}$$

$$\equiv C_{22}(x,z,t). \tag{A7}$$

At $z = 0$

$$(-K_z \frac{\partial C}{\partial z})_0 = a(t) e^{-\frac{u}{2K_x}x - \frac{v}{2K_y}y} e^{\left(\frac{u^2}{4K_x} + \frac{v^2}{4K_y} + \frac{w^2}{4K_z}\right)t}$$

$$-M e^{\frac{-u}{2K_x}x - \frac{v}{2K_y}y} e^{\left(\frac{u^2}{4K_x} + \frac{v^2}{4K_y} + \frac{w^2}{4K_z}\right)t}$$

$$-\, N C_{z=0}. \tag{A8}$$

where

$$N = N^* + \frac{w}{2} \tag{A8′}$$

At $z = D$

$$C = T_D e^{\frac{-u}{2K_x}x - \frac{v}{2K_y}y - \frac{w}{2K_z}D} e^{\left(\frac{u^2}{4K_x} + \frac{v^2}{4K_y} + \frac{w}{4K_z}\right)t}$$

$$\equiv C_D. \tag{A9}$$

Now consider sine transformation with respect to x and y:

$$\tilde{C}(z,t;k,m) = \int_0^{L_x} dx \int_0^{L_y} dy$$

$$\sin \frac{k\pi x}{L_x} \sin \frac{m\pi y}{L_y} C(x,y,z,t) \tag{A10a}$$

or the inverse transform:

$$C(x,y,z,t) = \frac{4}{L_x L_y} \sum_{k=1}^{\infty} \sum_{m=1}^{\infty} \tilde{C}(z,t;m,n)$$

$$\sin \frac{k\pi x}{L_x} \sin \frac{m\pi y}{L_y} \tag{A10b}$$

Multiplying (10), (11), (16), (17) by $\sin\ k\pi x/L_x$ $\sin\ m\pi y/L_y$, integrating over x and y, and using the boundary conditions (A4)-(A7), we obtain

$$\frac{\partial \tilde{C}}{\partial t} = K_z \frac{\partial^2 \tilde{C}}{\partial z^2} - \left(\frac{k^2\pi^2}{L_x^2} K_x + \frac{m^2\pi^2}{L_y^2} K_y\right)$$

$$\tilde{C} - \frac{k\pi}{L_x} K_x \left((-1)^k C_{12}^* - C_{11}^*\right)$$

$$- \frac{m\pi}{L_y} K_y \left((-1)^m C_{22}^{**} - C_{21}^{**}\right) \tag{A11}$$

At t = 0

$$\tilde{C} = \tilde{C}_0(z;k,m). \tag{A12}$$

At z = 0

$$(-K_z \frac{\partial \tilde{C}}{\partial z})_0 = \alpha(t;k,m) - N\, \tilde{C}_{z=0}. \tag{A13}$$

At z = D

$$\tilde{C} = \tilde{C}_D(t,k,m). \tag{A14}$$

where

$$C_{1j}^*(z,t,m) \equiv$$

$$\int_0^{L_y} C_{1j}(y,z,t) \sin\left(\frac{m\pi}{L_y} y\right) dy \quad (j = 1,2) \tag{A15}$$

$$C_{2j}^{**}(z,t,k) \equiv$$

$$\int_0^{L_x} C_{2j}(x,z,t) \sin\left(\frac{k\pi x}{L_x}\right) dx \quad (j = 1,2) \tag{A16}$$

$$\alpha(t;k,m) \equiv (a(t) - M) e^{\left(\frac{u^2}{4K_x} + \frac{v^2}{4K_y} + \frac{w^2}{4K_z}\right)t}$$

$$\int_0^{L_x} \int_0^{L_y} e^{-\frac{u}{2K_x}x - \frac{v}{2K_y}y}$$

$$\sin\left(\frac{k\pi}{L_x}x\right) \sin\left(\frac{m\pi}{L_y}y\right) dx dy \tag{A17}$$

and

$$\tilde{C}_D(t;k,m) \equiv T_D e^{\left(\frac{u^2}{4K_x} + \frac{v^2}{4K_y} + \frac{w^2}{4K_z}\right)t}$$

$$\int_0^{L_x} \int_0^{L_y} e^{-\frac{u}{2K_x}x - \frac{v}{2K_y}y}$$

$$\sin\left(\frac{k\pi}{L_x}x\right) \sin\left(\frac{m\pi}{L_y}y\right) dx dy \tag{A18}$$

Let

$$\tilde{C}(z,t;k,m) = \tilde{S}(z,t;k,m)e^{-\left(\frac{k^2\pi^2}{L_x^2}K_x+\frac{m^2\pi^2}{L_y^2}K_y\right)t} \quad \text{(A19)}$$

Substitution of (A19) into (A11)-(A14) leads to

$$\frac{\partial \tilde{S}}{\partial t} = K_z\frac{\partial^2 \tilde{S}}{\partial z^2} - R(z,t) \quad \text{(A20)}$$

At t = 0

$$\tilde{S} = \tilde{C}_0(z,k,m)$$

and at z = 0

$$-K_z\frac{\partial \tilde{S}}{\partial z}\,|_0 = \alpha(t;k,m)e^{\left(\frac{k^2\pi^2}{L_x^2}K_x+\frac{m^2\pi^2}{L_y^2}K_y\right)t} - N\,\tilde{S}\,,$$

or

$$\left(\tilde{S} - \frac{K_z}{N}\frac{\partial \tilde{S}}{\partial z}\right)_0 = \frac{\alpha(t)}{N}e^{\left(\frac{k^2\pi^2}{L_x^2}K_x+\frac{m^2\pi^2}{L_y^2}K_y\right)t} \quad \text{(A21)}$$

At z = D

$$\tilde{S} = \tilde{C}_D\, e^{\left(\frac{k^2\pi^2}{L_x^2}K_x+\frac{m^2\pi^2}{L_y^2}K_y\right)t} \quad \text{(A22)}$$

where

$$R(z,t) = \left[\frac{k\pi}{L_x}K_x\left((-1)^k C_{12}^{*} - C_{11}^{*}\right) + \frac{m\pi}{L_y}K_y\left((-1)^m C_{22}^{**} - C_{21}^{**}\right)\right]\cdot e^{\left(\frac{k^2\pi^2}{L_x^2}K_x+\frac{m^2\pi^2}{L_y^2}K_y\right)t} \quad \text{(A23)}$$

Letting

$$\tilde{S}(z,t;k,m) - \frac{K_z}{N}\frac{\partial \tilde{S}}{\partial z} \equiv \phi(z,t;k,m) \quad \text{(A24)}$$

we then reformulate the problem as follows:

$$\frac{\partial \phi}{\partial t} = K_z\frac{\partial^2 \phi}{\partial z^2} + R - \frac{K_z}{N}\frac{\partial R}{\partial z} \quad \text{(A25)}$$

with the boundary conditions

$$\phi(o,t) = \frac{\alpha(t)}{N}e^{\left(\frac{k^2\pi^2}{L_x^2}K_x+\frac{m^2\pi^2}{L_y^2}K_y\right)t} \equiv B_o(t) \quad \text{(A26)}$$

$$\phi(D,t) = \tilde{C}_D e^{\left(\frac{k^2\pi^2}{L_x^2}K_x+\frac{m^2\pi^2}{L_y^2}K_y\right)t} \equiv B_D(t) \quad \text{(A27)}$$

and the initial condition

$$\phi(o,z) = \tilde{C}_o(z;k,m) - \frac{K_z}{N}\frac{\partial}{\partial z}\tilde{C}_o(z;k,m) \equiv \phi_o(z). \quad \text{(A28)}$$

The system (A25)-(A28) can be solved analytically by the use of sine transformation. We define

$$\tilde{\phi}(n,t) \equiv \int_o^D \phi(z,t)\,\sin\,\frac{n\pi z}{D}dz \quad \text{(A29)}$$

$$\tilde{R}(n,t) \equiv \int_o^D R(z,t)\,\sin\,\frac{n\pi z}{D}dz \quad \text{(A30)}$$

Multiplying (A25) by sin $n\pi/D\ z$, and integrating with respect to z from $z=0$ to $z=D$, and using (A26) and (A27), we obtain

$$\frac{d\tilde{\phi}}{dt} = -\frac{n^2\pi^2K_z}{D^2}\tilde{\phi} + \frac{n\pi}{D}K_z\left(B_o(t) - (-1)^nB_D(t)\right) + \tilde{R} + \frac{n\pi K_z}{D\cdot N}\hat{R} \quad \text{(A31)}$$

where

$$\hat{R} = \int_0^D R(z,t)\,\cos\,\frac{n\pi z}{D}dz = \hat{R}(n,t) \quad \text{(A32)}$$

Equation (A31) can be solved using the transformed initial condition (A28). It results in

$$\tilde{\phi}(n,t) = \exp\left(\frac{-n^2\pi^2}{D^2}K_zt\right)\left[\tilde{\phi}_o(n) + \frac{n\pi K_z}{D}\int_o^t e^{\frac{n^2\pi^2}{D^2}K_zt'}\left(B_o(t') - (-1)^nB_D(t')\right)dt' + \int_o^t e^{\frac{n^2\pi^2}{D^2}K_zt'}\left(\tilde{R} + \frac{n\pi}{DN}K_z\hat{R}\right)dt'\right] \quad \text{(A33)}$$

The inverse transform of (A33) gives

$$\phi(z,t;k,m) = \frac{2}{D}\sum_{n=1}^{\infty}e^{-\frac{n^2\pi^2}{D^2}K_zt}\,\sin\,\frac{n\pi}{D}z\int_0^D \phi_o(z')\,\sin\,\frac{n\pi}{D}z'dz' + \frac{2\pi}{D^2}K_z\sum_{n=1}^{\infty}ne^{-\frac{n^2\pi^2}{D^2}K_zt}\,\sin\,\frac{n\pi}{D}z\int_0^t e^{\frac{n^2\pi^2}{D^2}K_zt'}\left(B_o(t') - (-1)^nB_D(t')\right)dt'$$

$$+\frac{2}{D}\sum_{n=1}^{\infty}e^{-\frac{n^2\pi^2}{D^2}K_zt}\,\sin\,\frac{n\pi}{D}z\int_0^t e^{\frac{n^2\pi^2}{D^2}K_zt'}dt'\int_0^D R(z',t')\,\sin\,\frac{n\pi}{D}z'dz' - \frac{2\pi}{D^2N}K_z\sum_{n=1}^{\infty}e^{-\frac{n^2\pi^2}{D^2}K_zt}\,\sin\,\frac{n\pi}{D}z\int_0^t e^{\frac{n^2\pi^2}{D^2}K_zt'}dt'\int_0^D R(z',t')\,\cos\,\frac{n\pi}{D}z'dz' \quad \text{(A34)}$$

The solution for $\tilde{S}$ is found by integrating (A24) with the substitution of (A34):

$$\tilde{S}(z,t) = \tilde{A}(t)e^{\frac{N}{K_z}z}$$

$$+ e^{\frac{N}{K_z}z} \int_0^z (-\frac{N}{K_z})\phi(z',t)e^{\frac{-N}{K_z}z'}dz' \qquad \text{(A35)}$$

where $\tilde{A}(t)$ is an integration constant (dependent on t and k, m). Using the lower boundary condition (A22), at $Z = D$ (A35) becomes

$$\tilde{S}(D,t) = \tilde{A}(t)e^{\frac{N}{K_z}D}$$

$$+ e^{\frac{N}{K_z}D} \int_0^D \left(-\frac{N}{K_z}\right)\phi(z',t)e^{-\frac{N}{K_z}z'}dz'$$

$$= \tilde{C}_D e^{\left(\frac{k^2\pi^2}{L_x^2}K_x + \frac{m^2\pi^2}{L_y^2}K_y\right)t} \qquad \text{(A36)}$$

Hence

$$\tilde{A}(t) = \tilde{C}_D e^{-\frac{N}{K_z}D} e^{\left(\frac{k^2\pi^2}{L_x^2}K_x + \frac{m^2\pi^2}{L_y^2}K_y\right)t}$$

$$+ \frac{N}{K_z}\int_o^D \phi(z',t)e^{-\frac{N}{K_z}z'}dz'. \qquad \text{(A37)}$$

Combining (A19), (A35) and (A37) with the inverse sine transformation, we solve for $C(x,y,z,t)$, and using (A1), we finally obtain an analytical solution (9).

Acknowledgments. The authors are grateful to C. Ho and B. Gussman for processing the data. This work has been supported by the Office of Naval Research through grants N00014-88K0207 and N0001491J1052. The first author also gratefully acknowledges the support provided under grants from the National Science Foundation (OCE-9116020), National Aeronautics and Space Administration (NAGW-2953), and National Oceanic and Atmospheric Administration (NA26GP0257-01 from the Global Change Program). This paper is contribution No. 851 from Marine Science Research Center, State University of New York, Stony Brook.

REFERENCES

Blumberg, A.F., and G.L. Mellor, A description of a three dimensional coastal ocean circulation model, in *Coastal Upwelling, Coastal and Estuarine Sci. Ser.* 4, edited by F.A. Richards, pp. 1-16, AGU, Washington, D.C., 1987.

Cayan, D.R., Variability of latent and sensible heat fluxes over the oceans, doctoral dissertation, 199 pp., Univ. of Calif., San Diego, 1990.

Cheney, R.E., B.C. Douglas, R.W. Agreen, L. Miller, D.L. Porter, and N.S. Doyle, Geosat altimeter geophysical data record users handbook, *NOAA Tech. Memo. NOS NGS-46*, NOAA, 29 pp., Natl. Ocean Serv., Office of Charting and Geodetic Serv., Rockville, Md., 1987.

Cheney, R.E., B.C. Douglas, R.W. Agreen, L. Miller, and N.S. Doyle, The NOAA Geosat geophysical data records: Summary of the first year of the exact repeat mission, *NOAA Tech. Memo. NOS NGS-48*, 20 pp., NOAA, Natl. Ocean Serv., Office of Charting and Geodetic Serv., Rockville, Md., 1988.

David, R.E., R. DeSzoeke, D. Halpern, and P. Niiler, Variability in the upper ocean during MILE, Part I, The heat and momentum balances, *Deep Sea Res. 28*, 1427-1451, 1981.

Emery, W.J., On the geographical variability of the upper level mean and eddy fields in the North Atlantic and North Pacific, *J. Phys. Oceanogr., 13*, 269-291, 1983.

Flament, P.L., L. Armi, and L. Washburn, The evolving structure of an upwelling filament, *J. Geophys. Res., 90*, 11,765-11,778, 1985.

Halpern, D., Observations of the deepening of the wind mixed layer in the northeast Pacific Ocean, *J. Phys. Oceanogr. 4*, 454-466, 1974.

Halpern, D., Observations of annual and El Niño thermal and flow variations at 0°, 110°W and 0°, 95°W during 1980-85, *J. Geophys. Res., 92*, 8197-8212, 1987.

Halpern, D., V. Zlotnicki, J. Newman, O. Brown, and F. Wentz, An atlas of monthly mean distributions of GEOSAT sea surface height, SSMI surface wind speed, AVHHR/2 sea surface temperature, and ECMWF surface wind components during 1988, *JPL Publ. 91-8*, 110 pp., 1991.

Holland, J. and X.-H. Yan, Remote sensing estimation of surface flow in the Delaware and New Jersey coastal region (abstract), *EOS Trans. AGU, 72*(17), suppl., 155, 1991.

Levitus, S., Climatological atlas of the world ocean. *NOAA Prof. Pap. 13*, 173 pp., U.S. Government Printing Office, Washington, D.C., 1982.

Liu, W.T., Moisture and latent heat flux variabilities in the tropical Pacific derived from satellite data, *J. Geophys. Res., 93*, 6749-6760, 1988.

Mellor, G.L., and T. Yamada, A hierarchy of turbulence closure models for planetary boundary layers, *J. Atmos. Sci., 31*, 1791-1800, 1974.

Price, J.F., R.A. Weller, and R. Pinkel, Diurnal cycling: Observations and models of the upper ocean response to diurnal heating, cooling, and wind mixing, *J. Geophys. Res., 91*(C7), 8411-8427, 1986.

Simpson, J.J., and R.J. Lynn, A mesoscale eddy dipole in the offshore California Current, *J. Geophys. Res., 95*, 13,009-13,022, 1990.

Wunsch, C., and E.M. Gaposchkin, On using satellite altimetry to determine the general circulation of the ocean with application to geoid improvement, *Rev. Geophys., 18*(4), 725-745, 1980.

Yan, X.-H., A. Bowman, and J. Schubel, Satellite observed spatial and temporal variability of the mixed layer depth in the Sargasso Sea, *Proc. of IEEE IGARSS*, vol. I, pp. 323-329, 1989.

Yan, X.-H., J. R. Schubel, and D. W. Pritchard, Oceanic upper mixed layer depth determination by the use of satellite data, *Remote Sens. Environ., 32*(1), 55-74, 1990*a*.

Yan, X.-H., P. Niiler, and R. Stewart, Possibility of using satellite observations for determining the structure of the mixed layer (abstract), *EOS Trans. AGU*, 71, suppl., 1420, 1990*b*.

Yan, X.-H., A. Okubo, J.R. Schubel, and D.W. Pritchard, An analytical mixed layer remote sensing, *Deep Sea Research, 38*(3), 267-287, 1991*a*.

Yan, X.-H., P.P. Niiler, and R.H. Stewart, Construction and accuracy analysis of images of the daily-mean mixed-layer depth, *Int. J. Rem. Sens., 12*(12), 2573-2584, 1991*b*

Akira Okubo, Marine Sciences Research Center, State University of New York, Stony Brook, NY 11794.

X.-H. Yan, Center for Remote Sensing, Graduate College of Marine Studies, University of Delaware, Newark, DE 19716.

(Received March 5, 1992;
revised June 18, 1992;
accepted July 27, 1992.)